



CHALMERS
UNIVERSITY OF TECHNOLOGY

Digging into the Interior of Hot Cores with the ALMA (DIHCA). III. The Chemical Link between NH_2CHO , HNCO , and

Downloaded from: <https://research.chalmers.se>, 2024-05-01 06:41 UTC

Citation for the original published paper (version of record):

Taniguchi, K., Sanhueza, P., Olguin, F. et al (2023). Digging into the Interior of Hot Cores with the ALMA (DIHCA). III. The Chemical Link between NH_2CHO , HNCO , and H_2CO . *Astrophysical Journal*, 950(1).
<http://dx.doi.org/10.3847/1538-4357/acca1d>

N.B. When citing this work, cite the original published paper.



Digging into the Interior of Hot Cores with the ALMA (DIHCA). III. The Chemical Link between NH_2CHO , HNCO , and H_2CO

Kotomi Taniguchi¹, Patricio Sanhueza^{1,2}, Fernando A. Olguin³, Prasanta Gorai⁴, Ankan Das⁵,

Fumitaka Nakamura^{1,2}, Masao Saito^{1,2}, Qizhou Zhang⁶, Xing Lu⁷, Shanghuo Li⁸, and Huei-Ru Vivien Chen³

¹ National Astronomical Observatory of Japan, National Institutes of Natural Sciences, 2-21-1 Osawa, Mitaka, Tokyo 181-8588, Japan; kotomi.taniguchi@nao.ac.jp

² Department of Astronomical Science, School of Physical Science, SOKENDAI (The Graduate University for Advanced Studies), Osawa, Mitaka, Tokyo 181-8588, Japan

³ Institute of Astronomy and Department of Physics, National Tsing Hua University, Hsinchu 30013, Taiwan

⁴ Department of Space, Earth and Environment, Chalmers University of Technology, SE-412 96, Gothenburg, Sweden

⁵ Institute of Astronomy Space and Earth Science, AJ 316, Salt lake, Sector II, Kolkata 700091, India

⁶ Center for Astrophysics | Harvard & Smithsonian, 60 Garden St., Cambridge, MA 02138, USA

⁷ Shanghai Astronomical Observatory, Chinese Academy of Sciences, 80 Nandan Road, Shanghai 200030, People's Republic of China

⁸ Max Planck Institute for Astronomy, Königstuhl 17, D-69117 Heidelberg, Germany

Received 2023 February 6; revised 2023 March 31; accepted 2023 March 31; published 2023 June 9

Abstract

We have analyzed the NH_2CHO , HNCO , H_2CO , and CH_3CN ($^{13}\text{CH}_3\text{CN}$) molecular lines at an angular resolution of $\sim 0''.3$ obtained by the Atacama Large Millimeter/submillimeter Array Band 6 toward 30 high-mass star-forming regions. The NH_2CHO emission has been detected in 23 regions, while the other species have been detected toward 29 regions. A total of 44 hot molecular cores (HMCs) have been identified using the moment 0 maps of the CH_3CN line. The fractional abundances of the four species have been derived at each HMC. In order to investigate pure chemical relationships, we have conducted a partial correlation test to exclude the effect of temperature. Strong positive correlations between NH_2CHO and HNCO ($\rho = 0.89$) and between NH_2CHO and H_2CO (0.84) have been found. These strong correlations indicate their direct chemical links; dual-cyclic hydrogen addition and abstraction reactions between HNCO and NH_2CHO and gas-phase formation of NH_2CHO from H_2CO . Chemical models including these reactions can reproduce the observed abundances in our target sources.

Unified Astronomy Thesaurus concepts: Astrochemistry (75); Interstellar molecules (849); Massive stars (732); Star formation (1569)

Supporting material: machine-readable tables

1. Introduction

Prebiotic molecules or precursors of organic matter, which are important for life, have been fervently explored in the interstellar medium (ISM) in recent years. Observations toward the molecular cloud G0.693-0.027 near the Galactic Center have reported the detection of molecules that are related to life; e.g., ethanolamine ($\text{NH}_2\text{CH}_2\text{CH}_2\text{OH}$; Rivilla et al. 2021a), cyanomethyl radical (HCNC ; Rivilla et al. 2021b), and (Z)-1,2-ethenediol ($(\text{CHOH})_2$; Rivilla et al. 2022). The detection of these species implies that the building blocks of life on Earth may have formed at the early stages of star formation. However, our current knowledge about the evolution of molecules, from simple molecules through the complex ones to biomolecules, is still lacking.

Formamide (NH_2CHO), the simplest possible amide, has been considered to be a potential prebiotic molecule (e.g., López-Sepulcre et al. 2019). This molecule contains a peptide bond that connects amino acids to form proteins. Its first detection in the ISM was achieved toward the Sagittarius B2 (Sgr B2) high-mass star-forming region (Rubin et al. 1971). More complex molecules including a peptide bond have been detected in the ISM; e.g., acetamide (CH_3CONH_2 ; Hollis et al. 2006) and N-methylformamide (CH_3NHCHO ; Belloche et al.

2017; Ligterink et al. 2020). Formamide could be related to these more complex molecules; thus it is important to reveal their chemistry in the ISM. Isocyanic acid (HNCO) has been considered as a precursor of NH_2CHO . It was first discovered in the ISM from Sgr B2 (Snyder & Buhl 1972), soon after the detection of NH_2CHO . Although their presence in the ISM has been known for 50 yr, their chemistry is still debated.

Tight correlations between NH_2CHO and HNCO have been found in observational studies. López-Sepulcre et al. (2015) derived a power-law relationship of $X(\text{NH}_2\text{CHO}) = 0.04X(\text{HNCO})^{0.93}$ from observational results toward young stellar objects (YSOs) with various stellar masses. Ligterink et al. (2020) investigated chemical links among several amide molecules toward the high-mass star-forming region NGC 6334I. They found that the $\text{HNCO}/\text{NH}_2\text{CHO}$ abundance ratios in this region are consistent with the average interstellar trend, and suggested that this result strengthens the probable link between HNCO and NH_2CHO . Law et al. (2021) investigated the spatial distribution of several complex organic molecules (COMs) toward the OB cluster-forming region G10.6-0.4, and found a spatial correlation between HNCO and NH_2CHO . Such a correlation supports that hydrogenation of HNCO on dust surfaces is a major formation route for NH_2CHO (e.g., Mendoza et al. 2014; López-Sepulcre et al. 2015, 2019; Song & Kästner 2016).

A gas-phase reaction between NH_2 and H_2CO has been investigated by quantum calculations and proposed as another formation route of NH_2CHO (Barone et al. 2015). This reaction has been found to be barrierless and can proceed even in low-



Original content from this work may be used under the terms of the [Creative Commons Attribution 4.0 licence](https://creativecommons.org/licenses/by/4.0/). Any further distribution of this work must maintain attribution to the author(s) and the title of the work, journal citation and DOI.

temperature conditions. Skouteris et al. (2017) reanalyzed this reaction and proposed an energy barrier of 4.88 K. As another formation route of NH_2CHO , solid-phase reactions have been investigated in laboratory experiments (e.g., Jones et al. 2011; Fedoseev et al. 2016; Dulieu et al. 2019; Martín-Doménech et al. 2020) and theoretical studies (e.g., Rimola et al. 2018; Enrique-Romero et al. 2019, 2022). For example, recent laboratory experiments showed that NH_2CHO forms in H_2O ice mixtures containing CO and NH_3 , irradiated by vacuum ultraviolet (VUV) photons (Chuang et al. 2022).

Recently, Lee et al. (2022) showed the spatial distribution of NH_2CHO , HNCO , and H_2CO , as well as other oxygen-bearing COMs, toward the atmosphere of the HH 212 protostellar disk. Although they found a similar abundance ratio as the star-forming regions studied in López-Sepulcre et al. (2019), they suggested that HNCO is likely formed in the gas phase and is a daughter molecule of NH_2CHO . The spatial distribution of H_2CO is more extended than that of NH_2CHO , and the gas-phase formation of NH_2CHO from the reaction between H_2CO and NH_2 is questionable from their observational data.

In contrast to the observational studies suggesting the chemical links between NH_2CHO and HNCO , Quénard et al. (2018) suggested that hydrogenation reaction of HNCO is unlikely to produce NH_2CHO on grain surfaces in their chemical models. They pointed out that the observed correlations between NH_2CHO and HNCO may come from the fact that they react to temperature in the same manner rather than a chemical link between them. Noble et al. (2015) also demonstrated that the hydrogenation reaction of HNCO fails to produce NH_2CHO efficiently in their laboratory experiments.

Gorai et al. (2020) analyzed data obtained with the Atacama Large Millimeter/submillimeter Array (ALMA) Band 4 toward the hot molecular core G10.47+0.03, and investigated the chemistry of molecules containing peptide-like bonds with chemical simulations. They found that HNCO and NH_2CHO are linked by the gas-phase dual-cyclic hydrogenation addition and abstraction reactions. They also proposed that the main formation route of NH_2CHO is the reaction between NH_2 and H_2CO in the warm-up and post-warm-up phases. If the findings of Gorai et al. (2020) are applicable to the general picture, we expect to find strong positive correlations between NH_2CHO and HNCO and between NH_2CHO and H_2CO in other star-forming regions. Nazari et al. (2022) investigated the correlation between HNCO and NH_2CHO using ALMA Band 6 data toward 37 high-mass sources with typical spatial resolutions of $0''.5$ – $1''.5$, corresponding to ~ 1000 – 5000 au. Although they found a correlation between them ($\rho = 0.73$), a caveat is that they used column densities that may also depend on the gas mass. Their observations do not include H_2CO , and therefore the relationship between NH_2CHO and H_2CO is still unclear.

In spite of several studies that have investigated the formation processes of NH_2CHO in star-forming regions, it is still an open question. In this paper, we present observations of the NH_2CHO , HNCO , H_2CO , and CH_3CN ($^{13}\text{CH}_3\text{CN}$) lines toward 30 high-mass star-forming regions covered by the “Digging into the Interior of Hot Cores with ALMA (DIHCA)” survey (Olguin et al. 2021, 2022). The typical angular resolution is $0''.3$. The source distances are between 1.3 and 5.26 kpc, resulting in linear resolutions of ~ 520 – 1590 au. The data sets used in this paper are described in Section 2. Moment 0 maps of molecular lines and their analyses are presented in

Sections 3.1 and 3.2, respectively. We discuss chemical relationships among NH_2CHO , HNCO , and H_2CO by statistical methods in Sections 4.1 and 4.2. The observed molecular abundances are compared with chemical models in Section 4.3. In Section 5, we summarize the main conclusions of this paper.

2. Observations

The 30 high-mass star-forming regions were observed by ALMA in band 6 (226.2 GHz, 1.33 mm) during cycles 4, 5, and 6 between 2016 and 2019 (Project IDs: 2016.1.01036.S, 2017.1.00237.S; PI: Sanhueza). Observations were performed using the 12 m array with a configuration similar to C40-5 and more than 40 antennas. The spectral configuration consists of four spectral windows of 1.8 GHz of width and a spectral resolution of 976 kHz ($\sim 1.3 \text{ km s}^{-1}$). These windows covered the frequency ranges of 233.5–235.5 GHz, 231.0–233.0 GHz, 216.9–218.7 GHz, and 219.0–221.0 GHz.

The observations were calibrated following the calibration procedure delivered by ALMA with CASA (CASA Team et al. 2022) versions 4.7.0, 4.7.2, 5.1.1-5, 5.4.0-70, and 5.6.1-8. The data were then self-calibrated in steps of decreasing solution time intervals. To obtain continuum-subtracted visibilities, we used the procedure from Olguin et al. (2021). Phase self-calibration was applied to the majority of the continuum-subtracted data sets to produce the data cubes. The data sets presented in this paper have angular resolutions of $0''.3$ – $0''.4$ with maximum recoverable scales between $8''$ and $11''$. The source selection criteria are as follows:

1. The source has a flux density of >0.1 Jy at 230 GHz.
2. The source distance (d) is between 1.6 kpc and 3.8 kpc. However, as parallax distances have been made available over time, some of the observed targets resulted to be closer, 1.3 kpc, and farther, 5.26 kpc.
3. The clump has an empirical mass–size threshold for high-mass star formation ($M > 580 M_\odot (r/\text{pc})^{1.33}$; Kauffmann & Pillai 2010; Sanhueza et al. 2017).

Further details on the source properties can be found in K. Ishihara et al. (2023, in preparation).

The imaging of the data cubes from the continuum-subtracted visibilities was performed with the automasking routine YCLEAN (Contreras 2018; Contreras et al. 2018). As part of YCLEAN several calls to the CASA task `tclean` were performed with a multiscale deconvolver and Briggs weighting with a robust parameter of 0.5. The estimated absolute calibration flux error is 10%, according to the ALMA Proposer’s User Guide.⁹

3. Results and Analyses

3.1. Moment 0 Maps

We constructed moment 0 maps of molecular lines. At first, we checked the spectra around continuum cores within a single beam size in each high-mass star-forming region and confirmed the detection of each molecular species. Information on lines used in the moment 0 maps that were checked for detection is summarized in Table 1. These lines are not blended with other lines in most of the target regions.

⁹ https://arc.iram.fr/documents/cycle4/ALMA_04_proposer_guide.pdf

Table 1
Information on Lines Used in Moment 0 Maps

Species	Transition ($J_{K_a,K_c} - J'_{K'_a,K'_c}$)	Frequency (GHz)	E_{up}/k (K)	Binding Energy ^a (K)	Binding Energy ^b (K)	Binding Energy ^c (K)
CH ₃ CN	$J_K = 12_3 - 11_3$	220.709017	133.16	4680	5906	4745–7652
NH ₂ CHO	$11_{3,9} - 10_{3,8}$	233.897318	94.16	5468	8104	5793–10,960
HNCO	$10_{0,10} - 9_{0,9}$	219.798274	58.02	4684
H ₂ CO	$3_{2,2} - 2_{2,1}$	218.475632	68.09	2050	5187	3071–6194

Notes.

^a Values of binding energy were calculated by Gorai et al. (2020).

^b Values of binding energy were calculated for crystalline ice by Ferrero et al. (2020).

^c Values of binding energy were calculated for amorphous nature to mimic the interstellar water ice mantles by Ferrero et al. (2020).

We present moment 0 maps (contour maps) overlaid on the continuum map (gray scale) in Figure 1 as an example. Moment 0 maps toward all of the regions are presented in Figures 9(a)–(d) in Appendix A. Information on noise levels and contour levels of each map are summarized in Tables 8 and 9 in Appendix A.

Emission of CH₃CN has been detected from all of the sources except for IRAS 18337-0743. In this source, no molecular lines have been detected. We therefore do not present the data toward this field in this paper. The detection rate of the CH₃CN line is 96.7% ($\frac{29}{30}$). We identified hot molecular cores (HMCs) based on the moment 0 maps of CH₃CN. If two or more HMCs have been identified in a high-mass star-forming region, we labeled numbers for HMCs in order of integrated intensity, from the highest to the lowest. We identified 44 HMCs in total over the 29 high-mass star-forming regions.

Emission of the H₂CO and HNCO lines has been detected from all of the high-mass star-forming regions, except for IRAS 18337-0743. Emission of NH₂CHO has been detected from 23 high-mass star-forming regions, and the detection rate is 76.7% ($\frac{23}{30}$).

Moment 0 maps of all of the molecular lines show almost similar peaks, and they are usually consistent with the continuum peaks within the beam size. The continuum emission of Band 6 mainly comes from dust emission in most of the sources. The G5.89-0.37 region is more evolved and shows unique features in both continuum and moment 0 maps. The continuum emission in this region is dominated by the free-free emission, and shows an explosive dispersal event (Fernández-López et al. 2021). These results imply that molecules are enhanced in shock regions produced by the expanding motion.

Spatial distributions of NH₂CHO are the most compact feature compared to the other species. This is expected, because the calculated binding energy of NH₂CHO is the highest among the observed species (see Table 1). We will discuss this point further in Section 4.2.

3.2. Analyses

We have conducted line identification and analyzed molecular lines at HMCs with the Markov Chain Monte Carlo (MCMC) method assuming the thermodynamics equilibrium (LTE) assumption in the CASSIS software (Vastel et al. 2015). The positions of HMCs are indicated as red crosses in the moment 0 maps (Figures 9(a)–(d)), and their exact positions are summarized in Table 8. The upper level energies, Einstein coefficients, degeneracies, and partition functions are taken from the CDMS database (for ¹³CH₃CN and CH₃CN; Endres et al. 2016) and

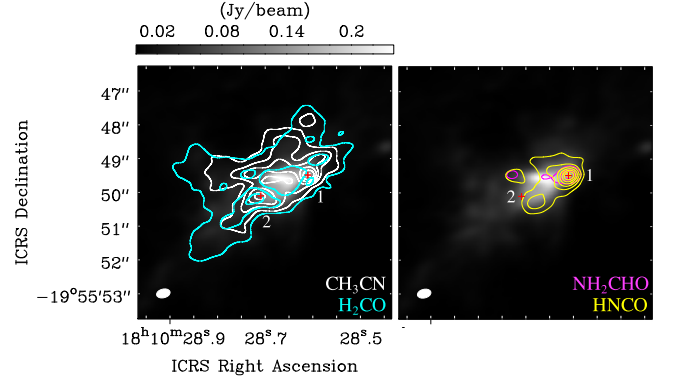


Figure 1. Continuum images (gray scales) overlaid with contours indicating the moment 0 maps of molecular lines (left panel: white; CH₃CN and cyan; H₂CO, right panel: magenta; NH₂CHO and yellow; HNCO) toward G10.62-0.38. Red crosses indicate the positions of hot molecular cores (HMCs) identified based on moment 0 maps of the CH₃CN line. Information on noise levels and contour levels are summarized in Tables 8 and 9.

the Jet Propulsion Laboratory (JPL) spectral line catalog (for NH₂CHO, HNCO, H₂CO; Pickett et al. 1998). The spectra were obtained within a single beam area.

In the line identification, we determined representative V_{LSR} values at each core using the data of the CH₃CN lines. We applied the representative V_{LSR} when we identified the lines of the other species, which enables us to pin down molecular lines in line-rich HMCs.

The column density (N), excitation temperature (T_{ex}), line width (FWHM), and systemic velocity (V_{LSR}) were treated as free parameters in the MCMC method. The size parameter was fixed, and then the beam filling factor was assumed to be one. We show the observed spectra (black curves) and the best-fitting model (red curves) toward the G10.62-0.38 HMC1 in Figure 2 as an example. We derived the excitation temperatures (T_{ex}) and column densities of ¹³CH₃CN by fitting its six K -ladder lines ($J_K = 13_K - 12_K$; $K = 0 - 5$, $E_{\text{up}}/k = 78.0 - 256.9$ K; see Table 2). We analyzed the ¹³CH₃CN spectra, instead of CH₃CN, because the low- K lines of the main isotopologue suffer from self absorption in some cases. The lines of ¹³CH₃CN are found to be optically thin ($\tau < 0.8$). The $J_K = 13_6 - 12_6$ line of ¹³CH₃CN has been detected in some sources, but this line could not be fitted well with the other lines simultaneously. This could happen, if emission of this line with a very high upper-state energy (335.5 K) comes from smaller regions than the other lines with lower upper-state energies. In general, the best-fitting models underestimate peak intensity of lines with high E_{up} . This is likely caused by a significant beam dilution effect, where emission of

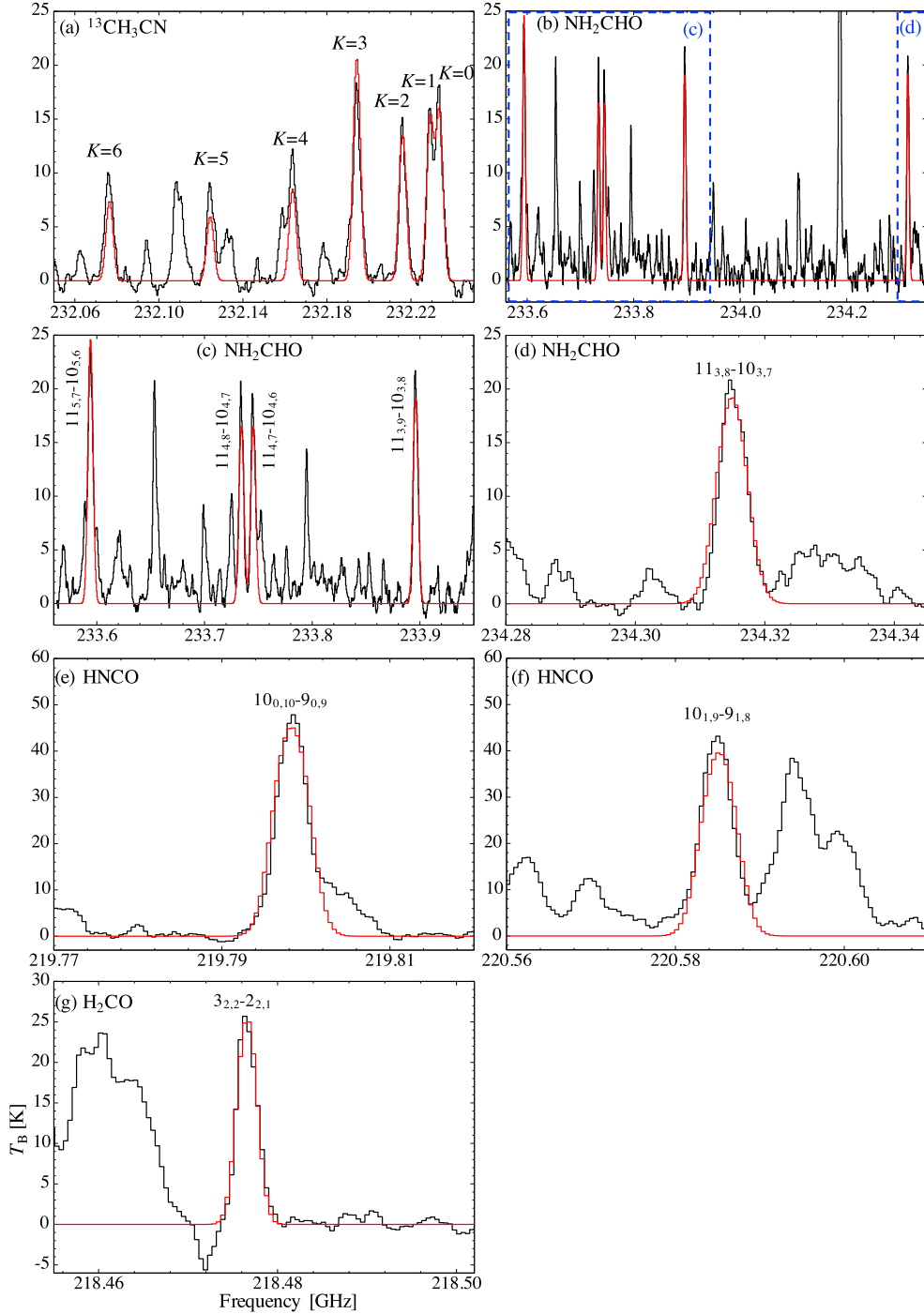


Figure 2. Spectra of molecular lines toward the G10.62-0.38 HMC1; (a) $^{13}\text{CH}_3\text{CN}$, (b)–(d) NH_2CHO (panels (c) and (d) are zoom-in spectra), (e) and (f) HNCO , and (g) H_2CO . Black and red curves indicate the observed spectra and best-fitting model, respectively. The blue dotted squares in panel (b) indicate the regions for panels (c) and (d), respectively.

higher E_{up} lines arises just in the hotter and inner region and does not fill up the observing beam. If the lines of $^{13}\text{CH}_3\text{CN}$ have not been detected (seven cores), we fitted the spectra of the K -ladder lines of CH_3CN ($J_K = 12_K - 11_K$; $K = 0 - 4$, $E_{\text{up}}/k = 68.9 - 183.1$ K; Table 2).

We converted the column densities of $^{13}\text{CH}_3\text{CN}$ to those of CH_3CN using the following formula (Yan et al. 2019):

$$^{12}\text{C}/^{13}\text{C} = 5.08D_{\text{GC}} + 11.86, \quad (1)$$

where D_{GC} (in kpc units) is the distance from the Galactic Center. The D_{GC} values are calculated from the galactic coordinate and the distance between the Sun and the Galactic center (8 kpc; Eisenhauer et al. 2003). We summarize the distance between the Sun and the target high-mass star-forming regions (D), D_{GC} , and the calculated $^{12}\text{C}/^{13}\text{C}$ ratio in Tables 3 and 4. Figure 3 shows the relationships between D_{GC} and the derived column density of CH_3CN . The Spearman's rank correlation coefficient (ρ) is derived to be +0.05. This means

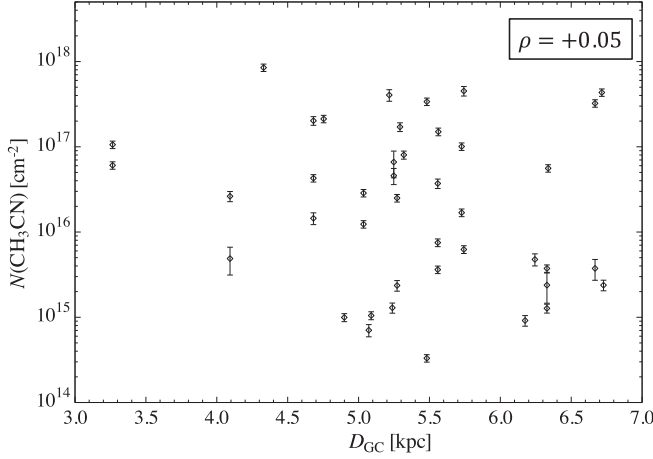


Figure 3. Relationships between the distance from the Galactic center (D_{GC}) and the column density of CH_3CN .

that no artificial effects occurred during the conversion from $N(^{13}\text{CH}_3\text{CN})$ to $N(\text{CH}_3\text{CN})$ and the conversion was successful.

The excitation temperature derived from $^{13}\text{CH}_3\text{CN}$ or CH_3CN is known to be a good thermometer (e.g., Hernández-Hernández et al. 2014; Hunter et al. 2014). In the case of the other species, several lines (see Table 2) with similar upper-state energies have been clearly detected, and it is difficult to determine their excitation temperatures and column densities simultaneously by fitting their lines. We then applied the values of excitation temperature derived from the analyses of $^{13}\text{CH}_3\text{CN}$ or CH_3CN . We checked the spectra at all of the positions and selected lines that can be clearly identified and are not affected by contamination by other lines in most positions.¹⁰ Table 2 summarizes information on lines used in the MCMC method. If the lines of the target species do not show the single Gaussian feature (e.g., possible contamination with other lines), we excluded them from the fitting to derive their column densities precisely. The derived column densities and excitation temperatures are summarized in Table 3. Assuming isothermal gas and using the excitation temperature derived from $^{13}\text{CH}_3\text{CN}$ or CH_3CN , we found all other lines to be optically thin. The results of V_{LSR} and FWHM derived by the MCMC method are summarized in Table 10 in Appendix B.

We derived the column densities of H_2 , $N(\text{H}_2)$, from the continuum data using the following formula (e.g., Sabatini et al. 2022):

$$N(\text{H}_2) = \frac{F_{1.3\text{mm}} \gamma}{B_{1.3\text{mm}}(T_{\text{dust}}) \Omega \kappa_{1.3\text{mm}} \mu_{\text{H}_2} m_{\text{H}}}, \quad (2)$$

where $F_{1.3\text{mm}}$, γ , $B_{1.3\text{mm}}(T_{\text{dust}})$, Ω , $\kappa_{1.3\text{mm}}$, μ_{H_2} , and m_{H} are the continuum peak flux at 1.3 mm, the gas-to-dust ratio, the Planck function at 1.3 mm with a dust temperature, the beam solid angle, the H_2 mean molecular weight (2.8), and the mass of the hydrogen atom, respectively. We adopted a value of $\kappa_{1.3\text{mm}} = 0.9 \text{ cm}^2 \text{ g}^{-1}$ (e.g., Ossenkopf & Henning 1994; Sanhueza et al. 2019; Sabatini et al. 2022). We assumed that the dust temperature is equal to the excitation temperature of $^{13}\text{CH}_3\text{CN}$ (or CH_3CN). The gas-to-dust ratios (γ) are calculated

¹⁰ Continuum subtraction could not be done successfully in NGC 6334I due to line forest. We then did not analyze molecular lines in this field.

Table 2
Information on Lines Used in MCMC Analyses

Species	Transition $J_{K_a, K_c} - J'_{K'_a, K'_c}$	Frequency (GHz)	E_{up}/k (K)	$\log A_{ij}$
$^{13}\text{CH}_3\text{CN}$	$J_K = 13_0 - 12_0$	232.234188	78.0	−2.9667
	$J_K = 13_1 - 12_1$	232.229822	85.2	−2.9693
	$J_K = 13_2 - 12_2$	232.216726	106.7	−2.9772
	$J_K = 13_3 - 12_3$	232.194906	142.4	−2.9907
	$J_K = 13_4 - 12_4$	232.164369	192.5	−3.0103
	$J_K = 13_5 - 12_5$	232.125130	256.9	−3.0368
CH_3CN	$J_K = 12_0 - 11_0$	220.747261	68.9	−3.0342
	$J_K = 12_1 - 11_1$	220.743011	76.0	−3.0372
	$J_K = 12_2 - 11_2$	220.730261	97.4	−3.0465
	$J_K = 12_3 - 11_3$	220.709017	133.2	−3.0624
NH_2CHO	$J_K = 12_4 - 11_4$	220.679287	183.1	−3.0857
	$11_{3,8} - 10_{3,7}$	234.316254	94.2	−3.06215
	$11_{3,9} - 10_{3,8}$	233.897318	94.1	−3.06449
	$11_{4,7} - 10_{4,6}$	233.746504	114.9	−3.09332
HNCO	$11_{4,8} - 10_{4,7}$	233.735603	114.9	−3.09334
	$11_{5,7} - 10_{5,6}$	233.595412	141.7	−3.13302
	$10_{0,10} - 9_{0,9}$	219.798320	58.0	−3.82082
H_2CO	$10_{1,9} - 9_{1,8}$	220.585200	101.5	−3.82055
	$3_{2,2} - 2_{2,1}$	218.475632	68.1	−3.80403

using the following formula (Giannetti et al. 2017):

$$\log(\gamma) = 0.087 D_{GC} + 1.44. \quad (3)$$

The continuum peak flux, gas-to-dust ratios, and derived H_2 column densities are summarized in Table 4.

4. Discussion

4.1. Correlation Among Each Species

We search for correlations among the observed species to investigate their chemical links. As mentioned in Section 1, NH_2CHO has been considered to be closely chemically linked with HNCO (e.g., López-Sepulcre et al. 2015, 2019). In addition, chemical simulations suggest gas-phase formation of NH_2CHO from H_2CO in hot core regions (Gorai et al. 2020). On the other hand, CH_3CN is not expected to be directly related to the other observed species.

We use abundances derived as $X(a) = N(a)/N(\text{H}_2)$, where a represents the molecular species, because comparisons using the column densities may mislead correlation coefficients. If we investigate correlations using column densities, the total gas mass or total gas column density represented by $N(\text{H}_2)$ could be the lurking third variable. We made plots to investigate this possibility as shown in Figure 4. The outliers, labeled as “IRAS 16562-3959 HMC2” and “IRAS 18162-2048,” show lower molecular column densities; nevertheless they have the highest H_2 column densities. IRAS 16562-3959 HMC2 is an ultracompact H II (UC H II) region (Guzmán et al. 2018; Taniguchi et al. 2020). IRAS 18162-2048 possesses a highly collimated magnetized radio jet (Carrasco-González et al. 2010). This jet may produce UV radiation via the strong shocks (Girart et al. 2017). Thus, the lower molecular column densities in these two sources are likely caused by destruction of molecules by the UV radiation.

We conducted the Spearman’s correlation coefficient test, and the derived p -values and correlation coefficients (ρ) are indicated in Figure 4. These statistical values mean that the molecular column densities have weak positive correlations with the H_2 column density. We then decided to use the

Table 3
Column Densities of Each Molecule Derived by the MCMC Method at Each Position

Region	Position	T_{ex} (K)	$N(^{13}\text{CH}_3\text{CN})$ ($\times 10^{13} \text{ cm}^{-2}$)	$^{12}\text{C}/^{13}\text{C}$	$N(\text{CH}_3\text{CN})$ ($\times 10^{14} \text{ cm}^{-2}$)	$N(\text{NH}_2\text{CHO})$ ($\times 10^{14} \text{ cm}^{-2}$)	$N(\text{HNCO})$ ($\times 10^{14} \text{ cm}^{-2}$)	$N(\text{H}_2\text{CO})$ ($\times 10^{15} \text{ cm}^{-2}$)
G10.62-0.38	HMC1	202.0 (1.2)	372 (37)	28	1058 (106)	170 (19)	719 (72)	60 (6)
	HMC2	199.4 (0.4)	213 (21)	28	606 (61)	...	78 (8)	120 (12)
G11.1-0.12	HMC	62.1 (0.3)	7.2 (0.7)	38	11 (1)	9.7 (1.0)	23 (2)	13 (1)
G11.92-0.61	HMC	212.0 (0.05)	590 (59)	36	2125 (213)	198 (22)	919 (92)	144 (50)
G14.22-0.50 S	HMC	80.29 (0.03)	...	43	9.2 (1.3)	4.7 (0.5)	19 (2)	14.9 (1.5)
G24.60+0.08	HMC	104.9 (0.1)	...	38	7.1 (1.2)	...	20 (2)	15.1 (1.5)
G29.96-0.02	HMC	270.4 (0.2)	2510 (251)	34	8489 (849)	1591 (178)	5687 (975)	872 (90)
G333.12-0.56	HMC1	193.6 (1.6)	65 (7)	39	250 (26)	27 (3)	110 (11)	25 (2)
	HMC2	73.3 (0.3)	6.11(0.9)	39	24 (3)	9.6 (1.0)	17 (2)	8.9 (0.9)
G333.23-0.06	HMC1	199.99 (0.01)	81 (11)	33	263 (36)	68 (7)	289 (46)	86 (9)
	HMC2	100.2 (0.1)	15 (5)	33	49 (18)	10.3 (1.6)	35 (3)	19 (2)
G333.46-0.16	HMC	111 (6)	19 (2)	40	75 (8)	...	9.4 (0.9)	11 (1)
	HMC1	150 (17)	93 (11)	40	371 (47)	42 (4)	119 (12)	16 (6)
	HMC2	113.3 (0.2)	9.0 (0.9)	40	36 (4)	13.0 (1.4)	52 (5)	25 (2)
G335.579-0.272	HMC	249.7 (0.1)	1055 (164)	38	4047 (629)	368 (40)	999 (100)	...
G335.78+0.17	HMC1	249.8 (0.1)	172 (59)	39	661 (229)	214 (21)	766 (90)	168 (17)
	HMC2	246 (2)	119 (16)	39	458 (98)	86 (9)	227 (30)	83 (8)
G336.01-0.82	HMC	218 (9)	207 (22)	39	803 (87)	202 (20)	619 (62)	...
G34.43+0.24	HMC	150.7 (0.3)	852 (85)	40	3385 (339)	426 (47)	1465 (158)	...
G34.43+0.24 MM2	HMC	116.6 (0.2)	...	40	3.3 (0.3)	...	3.25 (0.3)	7.6 (0.8)
G35.03+0.35A	HMC	218 (16)	78 (9)	44	48 (8)	64 (6)	238 (66)	97 (10)
G35.13-0.74	HMC1	100 (1)	54 (8)	44	37 (4)	41 (4)	58 (21)	...
	HMC2	175 (51)	...	44	24 (9)	10.9 (1.3)	44 (4)	24 (2)
	HMC3	92 (10)	...	44	12.7 (1.5)	7.5 (0.7)	19 (2)	14 (1)
G35.20-0.74 N	HMC	201.5 (0.7)	127 (13)	44	559 (56)	145 (15)	633 (63)	133 (14)
G351.77-0.54	HMC	165.3 (0.2)	943 (94)	46	4336 (434)	284 (28)
G5.89-0.37	HMC1	104 (2)	77 (8)	37	286 (29)	...	48 (5)	101 (10)
	HMC2	99.6 (0.2)	33 (3)	37	123 (12)	...	94 (9)	82 (8)
G343.12-0.06	HMC	226 (16)	441 (52)	39	1710 (201)	227 (91)	1440 (196)	403 (40)
IRAS 16562-3959	HMC1	149 (3)	246 (25)	41	1008 (102)	54 (5)	403 (40)	75 (44)
	HMC2	88 (8)	41 (4)	41	169 (17)	37 (4)	266 (27)	26 (3)
IRAS 18089-1732	HMC1	247 (21)	1100 (141)	41	4513 (578)	470 (48)	1646 (190)	201 (20)
	HMC2	79 (5)	15 (2)	41	62 (7)	14.0 (1.4)	39 (4)	35 (3)
IRAS 18151-1208	HMC	120 (14)	...	38	12.9 (1.7)	...	17 (2)	36 (4)
IRAS 18182-1433	HMC1	278 (15)	567 (66)	36	2022 (236)	391 (93)	1515 (154)	327 (30)
	HMC2	220.1 (0.7)	120 (12)	36	428 (43)	40 (8)	88 (17)	48 (5)
	HMC3	138 (20)	41 (6)	36	145 (23)	...	23 (2)	13.2 (1.3)
IRAS 18162-2048	HMC	94.3 (0.2)	...	46	24 (3)	...	50 (30)	28 (3)
IRDC 18223-1243	HMC	102 (5)	...	37	10.0 (1.1)	...	15 (2)	18 (2)
NGC6334I N	HMC1	176 (2)	707 (71)	46	3235 (324)	203 (20)	483 (179)	...
	HMC2	200.7 (0.3)	...	46	37 (10)	195 (20)	343 (122)	150 (15)
W33A	HMC	199 (5)	374 (39)	40	1501 (154)	405 (41)	3031 (452)	254 (25)

Note. The numbers in parentheses indicate errors including the standard deviation derived from the MCMC analysis and the absolute flux calibration error of 10%.

(This table is available in machine-readable form.)

abundances to investigate chemical relationships among molecular species in the following parts of this paper. Table 5 summarizes the derived abundances of each species, calculated from values summarized in Tables 3 and 4.

Figure 5 shows relationships between each pair of molecular species. We conducted the Spearman's rank correlation test for each pair. The Spearman's correlation coefficients (ρ) are derived to be 0.96 and 0.91 for pairs of NH_2CHO - HNCO and NH_2CHO - H_2CO , respectively. These high correlation coefficients imply that NH_2CHO may be chemically linked with HNCO and H_2CO . These results are consistent with the previous studies and the prediction by chemical simulations (Gorai et al. 2020).

We fitted the plot of NH_2CHO versus HNCO , as López-Sepulcre et al. (2015) analyzed. The best power-law fit is $X(\text{NH}_2\text{CHO}) = 0.07X(\text{HNCO})^{0.92(\pm 0.08)}$. López-Sepulcre et al. (2015) derived the best power-law fit as $X(\text{NH}_2\text{CHO}) =$

$0.04X(\text{HNCO})^{0.93}$, using data toward YSOs with various stellar masses, from low- through intermediate- to high-mass stars. Our result agrees with that derived by López-Sepulcre et al. (2015) well. Our data set contains a sample of targets with larger abundances of NH_2CHO ($\approx 3 \times 10^{-10} - 10^{-7}$) than those in López-Sepulcre et al. (2015; $\approx 3 \times 10^{-11} - 10^{-8}$), and our sample is the largest one in high-mass star-forming regions, to our best knowledge. The same best power-law fits for different ranges of abundances likely mean that the chemistry (formation and destruction processes) of NH_2CHO is common around YSOs with various stellar masses.

As we found a tight correlation between NH_2CHO and H_2CO , we also fitted the plot of NH_2CHO versus H_2CO with the same method. The best power-law fit is $X(\text{NH}_2\text{CHO}) = 0.35X(\text{H}_2\text{CO})^{1.07(\pm 0.09)}$.

Table 4
Distances, Gas-to-dust Ratio, Flux Density, and H₂ Column Density at Each Position

Region	Position	D (kpc)	D_{GC} (kpc)	γ	Peak Flux (mJy beam ⁻¹)	$N(\text{H}_2)$ ($\times 10^{23}$ cm ⁻²)
G10.62-0.38	HMC1	4.95	3.26	53	134	22 (2)
	HMC2	4.95	3.26	53	115	20 (2)
G11.1-0.12	HMC	3.0	5.09	76	7	33 (0.3)
G11.92-0.61	HMC	3.37	4.75	71	71	8.6 (0.9)
G14.22-0.50 S	HMC	1.9	6.17	95	25	11.3 (1.1)
G24.60+0.08	HMC	3.45	5.07	76	6	2.7 (0.3)
G29.96-0.02	HMC	5.26	4.33	66	96	15.0 (1.5)
G333.12-0.56	HMC1	3.3	5.27	79	27	4.0 (0.4)
	HMC2	3.3	5.27	79	14	5.9 (0.6)
G333.23-0.06	HMC1	5.2	4.09	63	30	3.4 (0.3)
	HMC2	5.2	4.09	63	80	19 (2)
G333.46-0.16	HMC	2.9	5.56	84	45	12.8 (1.3)
	HMC1	2.9	5.56	84	42	8.8 (0.9)
	HMC2	2.9	5.56	84	7	1.7 (0.2)
G335.579-0.272	HMC	3.25	5.22	78	274	31 (3)
G335.78+0.17	HMC1	3.2	5.25	79	100	11.4 (1.1)
	HMC2	3.2	5.25	79	30	3.5 (0.4)
G336.01-0.82	HMC	3.1	5.32	80	40	5.4 (0.5)
G34.43+0.24	HMC	3.5	5.48	83	236	48 (5)
G34.43+0.24 MM2	HMC	3.5	5.48	83	16	4.2 (0.4)
G35.03+0.35A	HMC	2.32	6.24	96	33	5.2 (0.5)
G35.13-0.74	HMC1	2.2	6.33	98	40	14.6 (1.5)
	HMC2	2.2	6.33	98	29	5.9 (0.6)
	HMC3	2.2	6.33	98	8	3.0 (0.3)
G35.20-0.74 N	HMC	2.19	6.34	98	77	13.7 (1.4)
G351.77-0.54	HMC	1.3	6.72	106	158	37 (4)
G5.89-0.37	HMC1	2.99	5.04	76	54	14.7 (1.5)
	HMC2	2.99	5.04	76	14	3.9 (0.4)
G343.12-0.06	HMC	2.9	5.29	80	168	22 (0.2)
IRAS 16562-3959	HMC1	2.38	5.73	87	10	4.0 (0.4)
	HMC2	2.38	5.73	87	155	102 (10)
IRAS 18089-1732	HMC1	2.34	5.74	87	157	20 (2)
	HMC2	2.34	5.74	87	26	11 (1)
IRAS 18151-1208	HMC	3.0	5.24	79	8	3.5 (0.4)
IRAS 18182-1433	HMC1	3.58	4.68	70	21	3.4 (0.3)
	HMC2	3.58	4.68	70	23	4.8 (0.5)
	HMC3	3.58	4.68	70	32	11 (1)
IRAS 18162-2048	HMC	1.3	6.73	106	319	134 (13)
IRDC 18223-1243	HMC	3.4	4.90	73	7	3.3 (0.3)
NGC6334I	HMC1	1.35	6.67	105	266	121 (12)
	HMC2	1.35	6.67	105	635	290 (29)
NGC6334I N	HMC1	1.35	6.67	105	141	55(5)
	HMC2	1.35	6.67	105	34	11 (1)
W33A	HMC	2.53	5.56	84	50	7.7 (0.8)

Note. The numbers in parentheses indicate errors calculated from the absolute flux calibration error of 10%.

(This table is available in machine-readable form.)

The second and third rows of Figure 5 show correlations between CH₃CN and NH₂CHO/HNCO/H₂CO. Although there are no expected direct chemical relationships between CH₃CN and the other species, there is a possibility that CH₃CN is positively correlated with the other species. The plots show more scatter compared to the two plots in the first row, suggestive of weaker correlations. The Spearman's correlation coefficients are derived to be 0.83, 0.85, and 0.74 for pairs of CH₃CN–NH₂CHO, CH₃CN–HNCO, and CH₃CN–H₂CO, respectively. These correlation coefficients are lower than those for pairs NH₂CHO–HNCO and NH₂CHO–H₂CO, but they still indicate strong correlations ($\rho \geq 0.7$). These correlations may mean that all of the species react to temperature in the same manner rather than chemical links

(Quénard et al. 2018). To explore this point further, we will consider a partial correlation test in the next subsection.

4.2. Partial Correlation Test

As we derived in Section 4.1, all of the species show positive correlations. However, as Quénard et al. (2018) pointed out, the observed correlations may not indicate chemical links, but they could reflect that all of the species act similarly against temperature. For example, assuming that molecules form on dust surfaces in the cold starless core stage and sublimate into the gas phase in the hot core regions with temperatures above 100 K, their abundances increase as the temperature increases. In this subsection, we will conduct a partial correlation test to investigate pure chemical links excluding the effect of temperature.

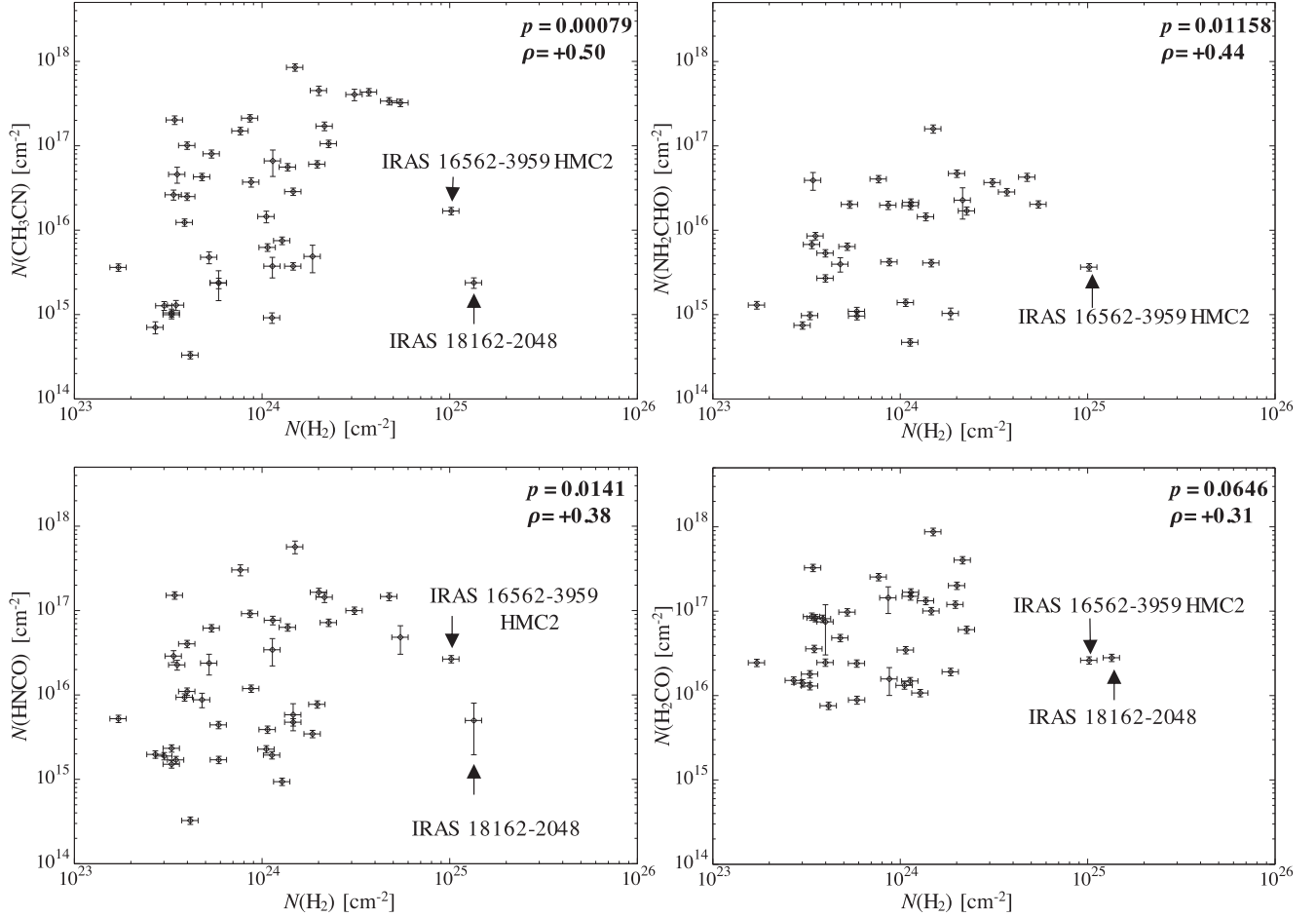


Figure 4. Relationships between the H_2 column density and molecular column densities.

Figure 6 shows relationships between excitation temperatures and molecular abundances. We found that all of the molecular abundances show positive correlations with the excitation temperatures; ρ values are 0.81, 0.78, 0.67, and 0.76 for NH_2CHO , HNCO , H_2CO , and CH_3CN , respectively. Hence, the correlation among each species derived in Section 4.1 may be fake, and the temperature may act as the lurking third variable.

In order to derive the pure chemical links excluding the lurking third variable, or the temperature, we conducted a partial correlation test. Assuming the local thermodynamic equilibrium (LTE), we use the excitation temperature derived from CH_3CN analyses to represent the gas kinetic temperature and dust temperature. The partial correlation test removes the mutual dependence of the two first variables on the third one. We utilize the excitation temperature derived from the analyses of the CH_3CN ($^{13}\text{CH}_3\text{CN}$) lines as a representative temperature. We adopted the first-order partial correlation coefficient (e.g., Wall & Jenkins 2012; Urquhart et al. 2018):

$$\rho_{12,3} = \frac{\rho_{12} - \rho_{13}\rho_{23}}{\sqrt{(1 - \rho_{13}^2)(1 - \rho_{23}^2)}}. \quad (4)$$

Here, we are interested in molecular abundances (1 and 2), and the temperature is considered as the third variable (3).

Table 6 summarizes all of the correlation coefficients for each pair of molecules. The derived partial correlation coefficients are summarized in the last row.

The partial correlation coefficients for HNCO – NH_2CHO and H_2CO – NH_2CHO are still high (>0.8), whereas those for the other pairs with CH_3CN become lower (<0.65). These results most likely indicate that NH_2CHO is chemically linked with HNCO and H_2CO . Thus, the observed correlation between NH_2CHO and HNCO is not the result of having the same response of the two species to temperature, as pointed out by Quénard et al. (2018). On the other hand, CH_3CN is less chemically linked with the other species studied here. We found that the partial correlation test is a strong tool to statistically investigate chemical relationships.

We further investigated the correlation coefficients between the molecular abundances and excitation temperatures. The highest correlation coefficient is derived for NH_2CHO (0.81), followed by HNCO (0.78), CH_3CN (0.76), and H_2CO (0.67). This order matches with the order of the calculated binding energies of each species (Table 1). This also suggests that thermal desorption is important for these molecules. As the emission of a molecule with a high binding energy should be dominated by the central hot core region, the correlation with the temperature should be strong. Hence, the derived correlation coefficients with the temperature suggest that the NH_2CHO emission comes from the central hot core region, whereas the emission of H_2CO could come not only from the inner hot core but also from the outer part of cores. This is consistent with the spatial distribution of the molecular lines (Figures 9(a)–(d)), as mentioned in Section 3.1.

Table 5
Molecular Abundances

Region	Position	$X(\text{CH}_3\text{CN})$	$X(\text{NH}_2\text{CHO})$	$X(\text{HNCO})$	$X(\text{H}_2\text{CO})$
G10.62-0.38	HMC1	$(4.7 \pm 0.7) \times 10^{-8}$	$(7.5 \pm 1.1) \times 10^{-9}$	$(3.2 \pm 0.4) \times 10^{-8}$	$(2.7 \pm 0.4) \times 10^{-8}$
	HMC2	$(3.1 \pm 0.4) \times 10^{-8}$...	$(3.9 \pm 0.6) \times 10^{-9}$	$(6.1 \pm 0.7) \times 10^{-8}$
G11.1-0.12	HMC	$(3.2 \pm 0.5) \times 10^{-9}$	$(3.0 \pm 0.4) \times 10^{-9}$	$(7.1 \pm 1.0) \times 10^{-9}$	$(3.9 \pm 0.6) \times 10^{-8}$
G11.92-0.61	HMC	$(2.5 \pm 0.3) \times 10^{-7}$	$(2.3 \pm 0.3) \times 10^{-8}$	$(1.1 \pm 0.2) \times 10^{-7}$	$(1.7 \pm 0.6) \times 10^{-7}$
G14.22-0.50 S	HMC	$(8.1 \pm 1.4) \times 10^{-10}$	$(4.2 \pm 0.6) \times 10^{-10}$	$(1.7 \pm 0.2) \times 10^{-9}$	$(1.3 \pm 0.2) \times 10^{-8}$
G24.60+0.08	HMC	$(2.6 \pm 0.5) \times 10^{-9}$...	$(7.3 \pm 1.0) \times 10^{-9}$	$(5.6 \pm 0.8) \times 10^{-8}$
G29.96-0.02	HMC	$(5.7 \pm 0.8) \times 10^{-7}$	$(1.1 \pm 0.2) \times 10^{-7}$	$(3.8 \pm 0.8) \times 10^{-7}$	$(5.8 \pm 0.8) \times 10^{-7}$
G333.12-0.56	HMC1	$(6.3 \pm 0.9) \times 10^{-8}$	$(6.8 \pm 1.0) \times 10^{-9}$	$(2.8 \pm 0.4) \times 10^{-8}$	$(6.2 \pm 0.9) \times 10^{-8}$
	HMC2	$(4.0 \pm 0.7) \times 10^{-9}$	$(1.6 \pm 0.2) \times 10^{-9}$	$(2.9 \pm 0.4) \times 10^{-9}$	$(1.5 \pm 0.2) \times 10^{-8}$
G333.23-0.06	HMC1	$(7.8 \pm 1.3) \times 10^{-8}$	$(2.0 \pm 0.3) \times 10^{-8}$	$(8.6 \pm 1.6) \times 10^{-8}$	$(2.6 \pm 0.4) \times 10^{-7}$
	HMC2	$(2.6 \pm 1.0) \times 10^{-9}$	$(5.6 \pm 1.0) \times 10^{-10}$	$(1.9 \pm 0.3) \times 10^{-9}$	$(1.0 \pm 0.1) \times 10^{-8}$
G333.46-0.16	HMC	$(5.9 \pm 0.8) \times 10^{-9}$...	$(7.3 \pm 1.0) \times 10^{-10}$	$(8.4 \pm 1.2) \times 10^{-9}$
	HMC1	$(4.2 \pm 0.7) \times 10^{-8}$	$(4.8 \pm 0.7) \times 10^{-9}$	$(1.4 \pm 0.2) \times 10^{-8}$	$(1.8 \pm 0.7) \times 10^{-8}$
	HMC2	$(2.1 \pm 0.3) \times 10^{-8}$	$(7.6 \pm 1.1) \times 10^{-9}$	$(3.0 \pm 0.4) \times 10^{-8}$	$(1.4 \pm 0.2) \times 10^{-7}$
G335.579-0.272	HMC	$(1.3 \pm 0.2) \times 10^{-7}$	$(1.2 \pm 0.2) \times 10^{-8}$	$(3.2 \pm 0.5) \times 10^{-8}$...
G335.78+0.17	HMC1	$(5.8 \pm 2.0) \times 10^{-8}$	$(1.9 \pm 0.3) \times 10^{-8}$	$(6.7 \pm 1.0) \times 10^{-8}$	$(1.5 \pm 0.2) \times 10^{-7}$
	HMC2	$(1.3 \pm 0.3) \times 10^{-7}$	$(2.4 \pm 0.3) \times 10^{-8}$	$(6.4 \pm 1.1) \times 10^{-8}$	$(2.4 \pm 0.3) \times 10^{-7}$
G336.01-0.82	HMC	$(1.5 \pm 0.2) \times 10^{-7}$	$(3.8 \pm 0.5) \times 10^{-8}$	$(1.2 \pm 0.2) \times 10^{-7}$...
G34.43+0.24	HMC	$(7.1 \pm 1.0) \times 10^{-8}$	$(9.0 \pm 1.3) \times 10^{-9}$	$(3.1 \pm 0.5) \times 10^{-8}$...
G34.43+0.24 MM2	HMC	$(8.0 \pm 1.1) \times 10^{-10}$...	$(7.8 \pm 1.1) \times 10^{-10}$	$(1.8 \pm 0.3) \times 10^{-8}$
G35.03+0.35A	HMC	$(9.1 \pm 1.7) \times 10^{-9}$	$(1.2 \pm 0.2) \times 10^{-8}$	$(4.6 \pm 1.3) \times 10^{-8}$	$(1.9 \pm 0.3) \times 10^{-7}$
G35.13-0.74	HMC1	$(2.6 \pm 0.4) \times 10^{-9}$	$(2.8 \pm 0.4) \times 10^{-9}$	$(4.0 \pm 1.5) \times 10^{-9}$...
	HMC2	$(4.1 \pm 1.6) \times 10^{-9}$	$(1.9 \pm 0.3) \times 10^{-9}$	$(7.5 \pm 1.1) \times 10^{-9}$	$(4.1 \pm 0.6) \times 10^{-8}$
	HMC3	$(4.2 \pm 0.7) \times 10^{-9}$	$(2.5 \pm 0.4) \times 10^{-9}$	$(6.3 \pm 0.9) \times 10^{-9}$	$(4.7 \pm 0.7) \times 10^{-8}$
G35.20-0.74 N	HMC	$(4.1 \pm 0.6) \times 10^{-8}$	$(1.1 \pm 0.2) \times 10^{-8}$	$(4.6 \pm 0.7) \times 10^{-8}$	$(9.7 \pm 1.4) \times 10^{-8}$
G351.77-0.54	HMC	$(1.2 \pm 0.3) \times 10^{-7}$	$(7.7 \pm 1.1) \times 10^{-9}$
G5.89-0.37	HMC1	$(2.0 \pm 0.2) \times 10^{-8}$...	$(3.2 \pm 0.5) \times 10^{-9}$	$(6.9 \pm 1.0) \times 10^{-8}$
	HMC2	$(3.2 \pm 0.5) \times 10^{-8}$...	$(2.4 \pm 0.3) \times 10^{-8}$	$(2.1 \pm 0.3) \times 10^{-7}$
G343.12-0.06	HMC	$(8.0 \pm 1.2) \times 10^{-8}$	$(1.1 \pm 0.4) \times 10^{-8}$	$(6.7 \pm 1.1) \times 10^{-8}$	$(1.9 \pm 0.3) \times 10^{-7}$
IRAS 16562-3959	HMC1	$(2.5 \pm 0.4) \times 10^{-7}$	$(1.3 \pm 0.2) \times 10^{-8}$	$(1.0 \pm 0.1) \times 10^{-7}$	$(1.9 \pm 1.1) \times 10^{-7}$
	HMC2	$(1.7 \pm 0.2) \times 10^{-9}$	$(3.6 \pm 0.5) \times 10^{-10}$	$(2.6 \pm 0.4) \times 10^{-9}$	$(2.6 \pm 0.4) \times 10^{-9}$
IRAS 18089-1732	HMC1	$(2.3 \pm 0.4) \times 10^{-7}$	$(2.3 \pm 0.3) \times 10^{-8}$	$(8.2 \pm 1.3) \times 10^{-8}$	$(1.0 \pm 0.1) \times 10^{-7}$
	HMC2	$(5.8 \pm 0.8) \times 10^{-9}$	$(1.3 \pm 0.2) \times 10^{-9}$	$(3.6 \pm 0.5) \times 10^{-9}$	$(3.2 \pm 0.5) \times 10^{-8}$
IRAS 18151-1208	HMC	$(3.7 \pm 0.6) \times 10^{-9}$...	$(4.9 \pm 0.7) \times 10^{-9}$	$(1.0 \pm 0.2) \times 10^{-7}$
IRAS 18182-1433	HMC1	$(5.9 \pm 0.9) \times 10^{-7}$	$(1.1 \pm 0.3) \times 10^{-7}$	$(4.4 \pm 0.6) \times 10^{-7}$	$(9.5 \pm 1.4) \times 10^{-7}$
	HMC2	$(9.0 \pm 1.3) \times 10^{-8}$	$(8.3 \pm 1.8) \times 10^{-9}$	$(1.8 \pm 0.4) \times 10^{-8}$	$(1.0 \pm 0.2) \times 10^{-7}$
	HMC3	$(1.4 \pm 0.3) \times 10^{-8}$...	$(2.2 \pm 0.3) \times 10^{-9}$	$(1.3 \pm 0.2) \times 10^{-8}$
IRAS 18162-2048	HMC	$(1.8 \pm 0.3) \times 10^{-10}$...	$(3.7 \pm 2.3) \times 10^{-10}$	$(2.1 \pm 0.3) \times 10^{-9}$
IRDC 18223-1243	HMC	$(3.0 \pm 0.4) \times 10^{-9}$...	$(4.6 \pm 0.6) \times 10^{-9}$	$(5.4 \pm 0.8) \times 10^{-8}$
NGC6334I N	HMC1	$(5.9 \pm 0.8) \times 10^{-8}$	$(3.7 \pm 0.5) \times 10^{-9}$	$(8.8 \pm 3.4) \times 10^{-9}$	
	HMC2	$(3.3 \pm 1.0) \times 10^{-9}$	$(1.7 \pm 0.2) \times 10^{-8}$	$(3.0 \pm 1.1) \times 10^{-8}$	$(1.3 \pm 0.2) \times 10^{-7}$
W33A	HMC	$(2.0 \pm 0.2) \times 10^{-7}$	$(5.3 \pm 0.7) \times 10^{-8}$	$(4.0 \pm 0.6) \times 10^{-7}$	$(3.3 \pm 0.5) \times 10^{-7}$

Note. Errors include the standard deviation derived from the MCMC analysis and the absolute flux calibration error of 10%.

(This table is available in machine-readable form.)

4.3. Comparison with Chemical Models

We compare the observed molecular abundances with the chemical models developed by Gorai et al. (2020). We consider a linear density variation with a slope $\frac{\rho_{\text{max}} - \rho_{\text{min}}}{t_f - t_i}$, where $t_f - t_i$ corresponds to the collapse timescale. Similarly, the temperature increases with a linear slope during the warm-up stage.

The dual-cyclic hydrogen addition and abstraction reactions (Haupa et al. 2019) that occur in the gas phase are included in the models. This cycle consists of four reactions. From HNCO to NH_2CHO , two hydrogen addition reactions occur:



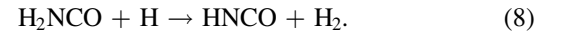
followed by



In a sequence from NH_2CHO to HNCO, two hydrogen abstraction reactions happen:



followed by



Reactions (6) and (8) are barrierless, whereas Reactions (5) and (7) have activation barriers of 2530–5050 K and 240–3130 K, respectively. In the models of Gorai et al. (2020), the gas-phase reaction between NH_2 and H_2CO to form NH_2CHO is included:



The hydrogenation reaction leads to the formation of CH_3CN on dust surfaces in the cold phase. In contrast, its formation by a dust-surface radical–radical reaction between CN and CH_3 is

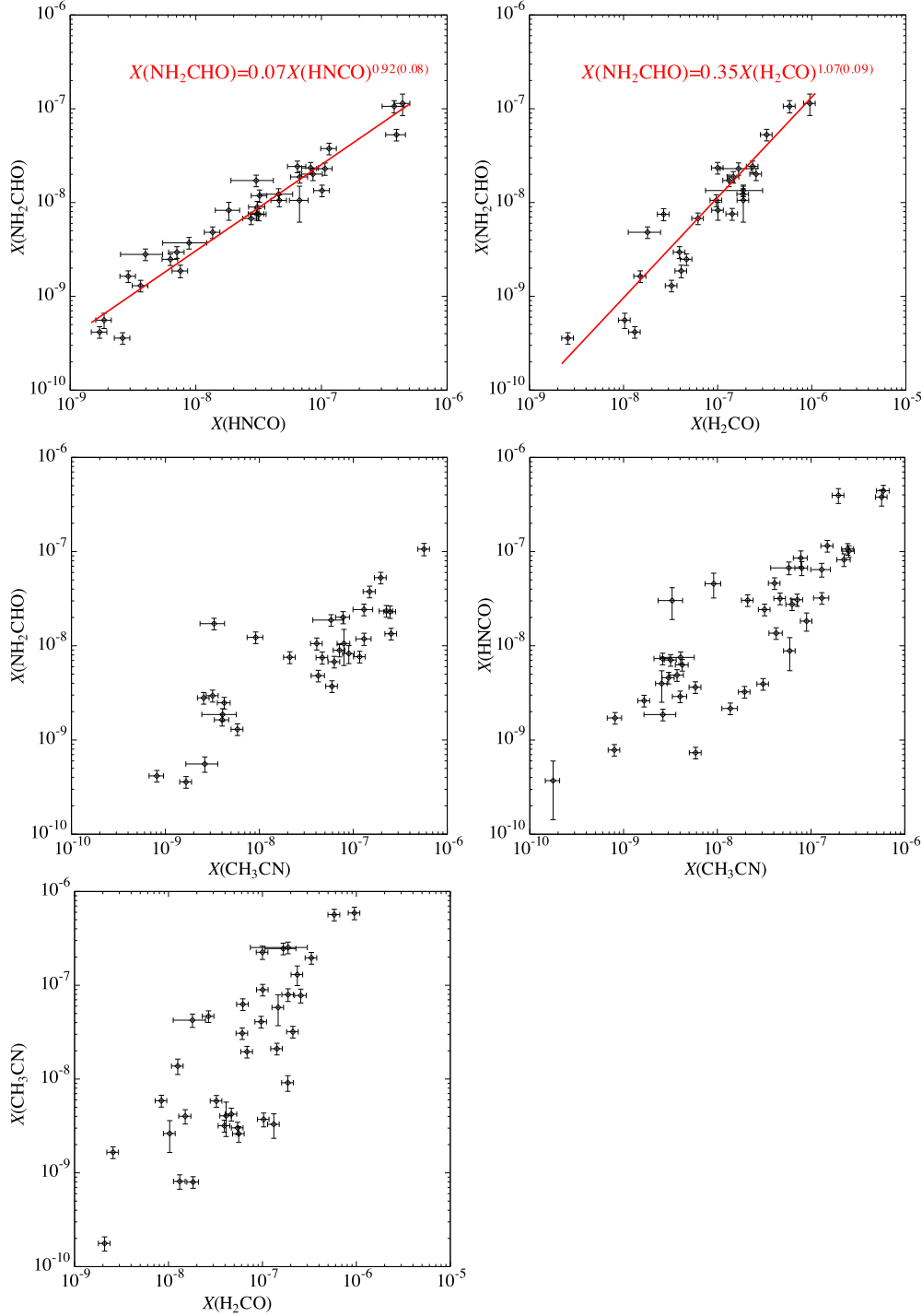


Figure 5. Relationships of molecular abundances. The red lines in the top two panels show the result of the best power-law fit.

efficient during the initial warm-up phase. In addition, CH_3CN could form by the following barrierless reaction on dust surfaces:



The major gas-phase formation route of CH_3CN is the dissociative recombination reaction of CH_3CNH^+ . Destruction routes of CH_3CN on dust surfaces are cosmic-ray-induced desorption, photodissociation, and thermal and nonthermal desorption. Furthermore, the models of Gorai et al. (2020)

include the successive hydrogenation reactions of CH_3CN to lead finally to ethanimine (CH_3CHNH).

There are six physical parameters in the models of Gorai et al. (2020); the maximum density (ρ_{max} [cm^{-3}]), maximum temperature (T_{max} [K]), collapsing timescale (t_{coll} [yr]), warm-up timescale (t_{w} [yr]), post-warm-up timescale (t_{pw} [yr]), and initial dust temperature (T_{ice} [K]). Gorai et al. (2020) ran two types of models, Model A and Model B, as summarized in Table 9 in their paper. In Model A, the physical parameters are fixed with the following values; $\rho_{\text{max}} = 10^7 \text{ cm}^{-3}$, $T_{\text{max}} = 200 \text{ K}$, $t_{\text{coll}} = 10^6 \text{ yr}$, $t_{\text{w}} = 5 \times 10^4 \text{ yr}$, $t_{\text{pw}} = (6.2\text{--}10) \times 10^4 \text{ yr}$, and

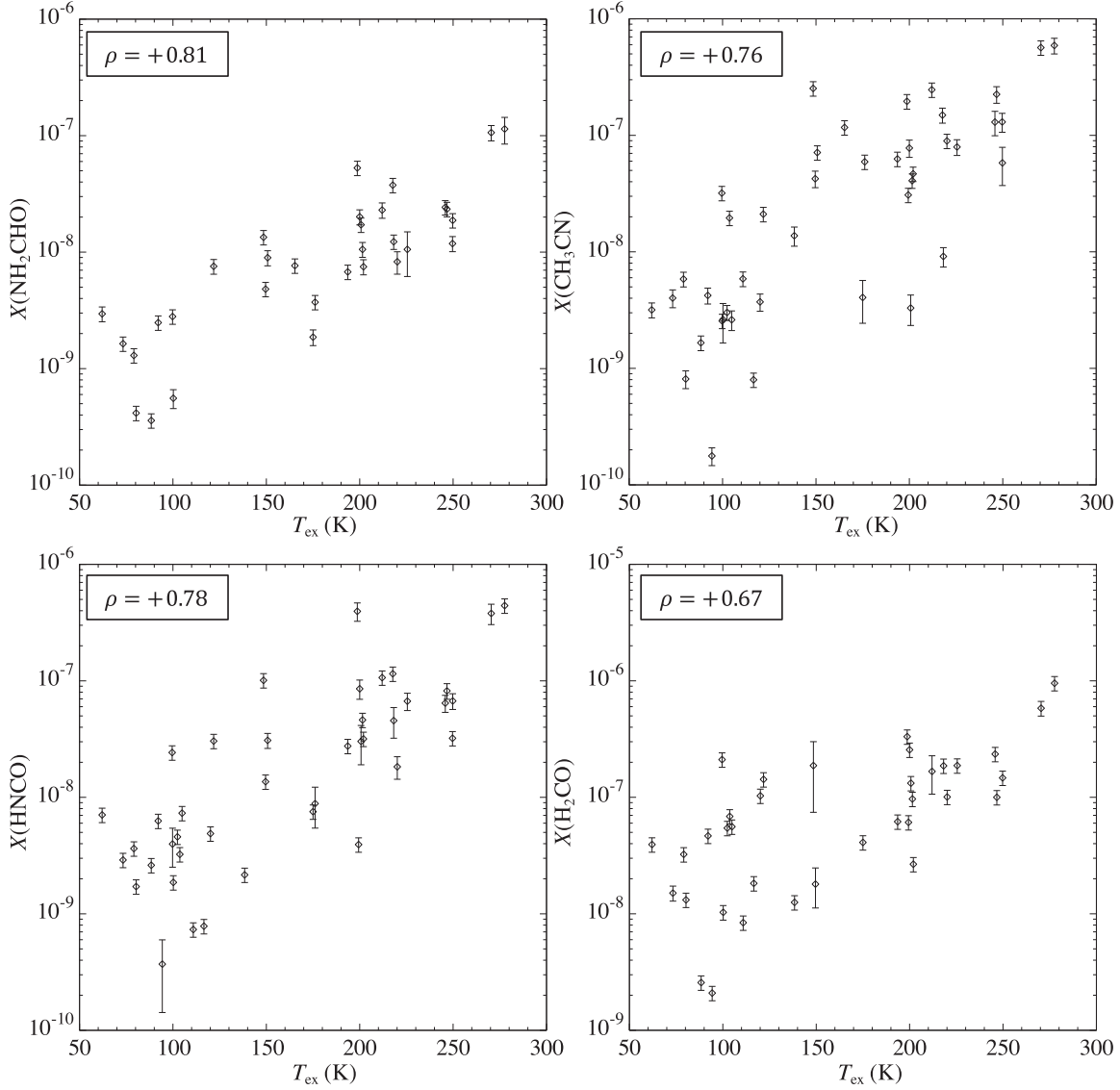


Figure 6. Relationships between excitation temperatures and molecular abundances.

Table 6
Summary of Partial Correlation Coefficient

	HNCO versus NH ₂ CHO	H ₂ CO versus NH ₂ CHO	CH ₃ CN versus HNCO	CH ₃ CN versus NH ₂ CHO	H ₂ CO versus CH ₃ CN
ρ_{12}	0.96	0.91	0.85	0.83	0.74
ρ_{13}	0.78	0.67	0.76	0.76	0.67
ρ_{23}	0.81	0.81	0.78	0.81	0.76
$\rho_{12,3}$	0.89	0.84	0.64	0.55	0.48

Note. “1” and “2” correspond to Species A and Species B, respectively (Species A versus Species B written at the top of table). “3” corresponds to the excitation temperature.

$T_{\text{ice}} = 20$ K. For Model B, ρ_{max} , T_{max} , and t_{coll} varied in ranges of 10^5 – 10^7 cm⁻³, 100–400 K, and 10^5 – 10^6 yr, respectively. The warm-up timescale, post-warm-up timescale, and initial dust temperatures were fixed at 5×10^4 yr, 10^5 yr, and 20 K, respectively, in Model B.

Figure 7 shows comparisons between the observed abundances and the modeled abundances obtained by Model A (Gorai et al. 2020). As the observed values, we plot the four representative values from the whole hot core populations; maximum, average, median, and minimum values (Table 7).

The minimum abundances agree with the model around 1.02×10^6 yr ($T \approx 100$ K). The minimum observed CH₃CN abundance agrees with model at the almost same age within a factor of 1.3. The minimum abundance of NH₂CHO is derived at IRAS 16562-3959 HMC2, and those of HNCO and H₂CO are derived in IRAS 18162-2048. The derived excitation temperatures of CH₃CN in these HMCs are 88 K and 94.3 K, which are lower than the other sources and close to the modeled value of 100 K. In addition, in the case of IRAS 18162-2048, as mentioned before, the ionized jet may explain the lower molecular column densities.

The observed average and median abundances of HNCO and NH₂CHO are most close to the modeled values around $(\approx 1.04\text{--}1.05) \times 10^6$ yr ($T \approx 165\text{--}200$ K). The temperature ranges that can reproduce the observed average and median values agree with the average excitation temperature at the whole hot core

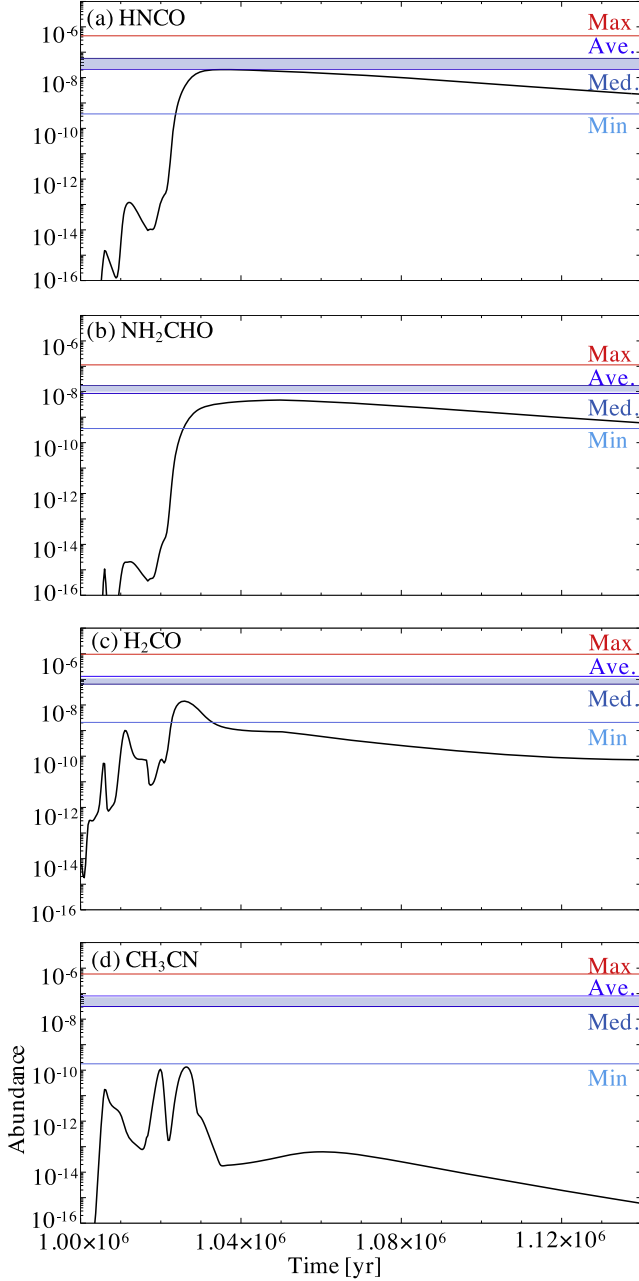


Figure 7. Comparison with Model A (Gorai et al. 2020). Panels (a)–(d) show results of HNCO, NH₂CHO, H₂CO, and CH₃CN, respectively. Black curves indicate the modeled abundances (gas phase). The four representative observed abundances are plotted (Maximum, Average, Median, and Minimum). The blue filled ranges indicate the ranges between average and median values.

populations (≈ 162 K). Thus, the tendencies of the observed abundances for both HNCO and NH₂CHO agree with the modeled results. The median value of H₂CO is close to the modeled abundance around $\approx 1.03 \times 10^6$ yr, which is almost consistent with the ages constrained by HNCO and NH₂CHO (≈ 1.04 – 1.05×10^6 yr), but in general, the modeled H₂CO abundances tend to be lower than the observed ones. The observed maximum abundances cannot be explained by Model A, implying that assumed physical parameters are not suitable for the hot core with the maximum molecular abundances.

Figure 8 shows a comparison between the representative observed abundances and modeled abundances obtained by

Model B (Gorai et al. 2020). The left panels show the dependences on different t_{coll} and ρ_{max} , and the right panels show the dependences on different t_{coll} and T_{max} , respectively. The initial dust temperature (T_{ice}) is fixed at 20 K, and t_{pw} is 10^5 yr. The modeled abundances plotted here are the values at the end of the simulations; $t = t_{\text{collapse}} + t_{\text{warm-up}} (5 \times 10^4 \text{ yr}) + t_{\text{post warm-up}} (10^5 \text{ yr})$. As seen in Figure 8, the maximum observed abundances could not be reproduced by the models in most cases, because the plotted modeled abundances are the values at the end of the simulation. We show the modeled maximum abundances obtained by Model B in Figure 10 in Appendix C. The modeled maximum abundances with some cases consist with the observed maximum abundances by less than 1 order of magnitude.

In Figure 8, we found low abundances of H₂CO and high abundances of NH₂CHO in the models. We attribute these results to the uncertainty of the reaction rate coefficient for the gas-phase reaction between NH₂ and H₂CO (Reaction (9)). We used an α value of 5.00×10^{-12} , but Skouteris et al. (2017) derived a value of 7.79×10^{-15} by their quantum chemical calculation. However, the γ value provided by Skouteris et al. (2017) was ≈ 5.5 times lower than that of Barone et al. (2015). Here, we used the γ value from Skouteris et al. (2017). If the α value for this reaction becomes lower, as suggested by Skouteris et al. (2017), the conversion rate from H₂CO to NH₂CHO should be slow. In addition to the α , β and γ values used in Gorai et al. (2020) for this reaction, we have also evaluated the modeling results considering the α , β , and γ values available in Skouteris et al. (2017). We did not find significant changes for our best-fit results that are obtained comparing with observation. Only a minor change in collapsing time has been noticed.

The maximum abundances of HNCO and NH₂CHO can be reproduced by the models with $\rho_{\text{max}} = 10^5$ – $10^{6.5} \text{ cm}^{-3}$, as seen in the left panels. The average and median abundances of these two species agree with the following three models; (1) $\rho_{\text{max}} = 10^6 \text{ cm}^{-3}$ and $t_{\text{coll}} \approx 8 \times 10^5 \text{ yr}$, (2) $\rho_{\text{max}} = 10^{6.5} \text{ cm}^{-3}$ and $t_{\text{coll}} = 4 \times 10^5 \text{ yr}$, and (3) $\rho_{\text{max}} = 10^7 \text{ cm}^{-3}$ and $t_{\text{coll}} = 2 \times 10^5 \text{ yr}$. The models with higher ρ_{max} values need to collapse rapidly to reproduce the observed abundances. Their minimum abundances cannot be reproduced by the models, because the adopted maximum temperature (200 K) is too high for these sources (88–95 K; see in the previous paragraph). In fact, the minimum abundances can be reproduced by the model with $T_{\text{max}} = 100 \text{ K}$ in the right panels, as discussed later.

The minimum H₂CO abundance is reproduced by the models with $\rho_{\text{max}} = 10^{6.5}$ – 10^7 cm^{-3} , while the average and median values agree with the model with $\rho_{\text{max}} = 10^{5.5} \text{ cm}^{-3}$. In addition, the models with $\rho_{\text{max}} = 10^5 \text{ cm}^{-3}$ and 10^6 cm^{-3} reproduce the average and median abundances around $t_{\text{coll}} \approx (1$ – $2) \times 10^5 \text{ yr}$. The observational results of H₂CO tend to show agreements with lower- ρ_{max} models compared to the cases of HNCO and NH₂CHO ($\rho_{\text{max}} = 10^6$ – 10^7 cm^{-3}). These results would be consistent with the fact that the H₂CO emission shows more spatially extended features than the other molecules (Figures 9(a)–(d) in Appendix A). The maximum value, derived in IRAS 18182-1433 HMC1, has not been reproduced by the models in Figure 8, but the modeled maximum abundances with $\rho_{\text{max}} = 10^5 \text{ cm}^{-3}$ agree with the observed maximum value within 1 order of magnitude (see Figure 10 in Appendix C).

As seen in the right panels of HNCO and NH₂CHO in Figure 8, the maximum abundances prefer shorter collapsing time with a highest T_{max} of 400 K. The maximum abundances of the

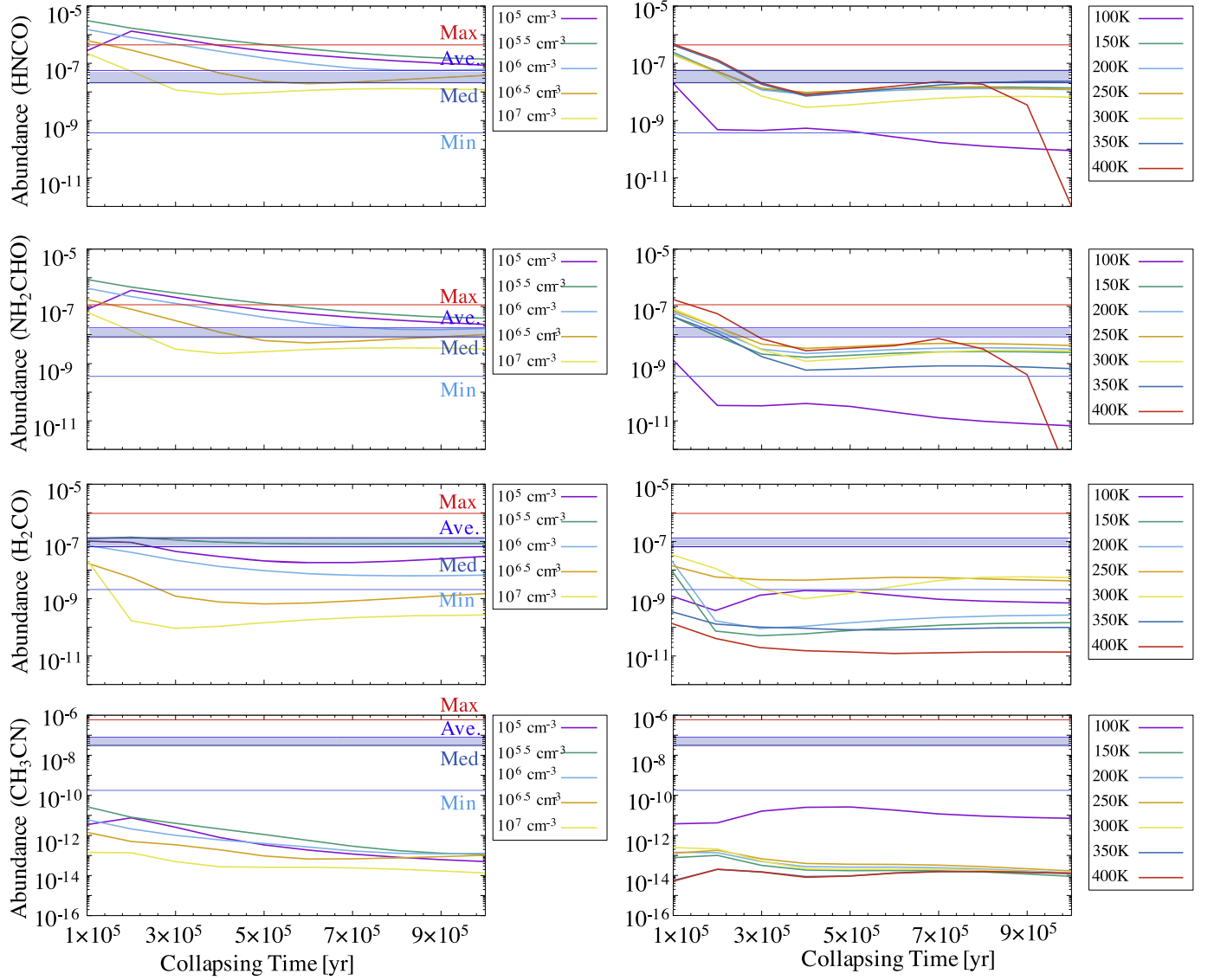


Figure 8. Comparison with Model B (Gorai et al. 2020). The panels from top to bottom show the results of HNCO, NH₂CHO, H₂CO, and CH₃CN, respectively. The modeled abundances plotted here are the values at the end of the simulations; $t = t_{\text{collapse}} + t_{\text{warm-up}} (5 \times 10^4 \text{ yr}) + t_{\text{post warm-up}} (10^5 \text{ yr})$. The left panels show the dependences on different collapsing timescales and maximum densities with a maximum temperature of 200 K. The right panels show the dependences on different collapsing timescales and maximum temperatures with a maximum density of 10^7 cm^{-3} . The four representative observed abundances are plotted (Maximum, Average, Median, and Minimum). The blue filled ranges indicate the ranges between average and median values.

Table 7
Summary of Representative Observed Abundances

	HNCO	NH ₂ CHO	H ₂ CO	CH ₃ CN
Minimum (Min)	3.70×10^{-10}	3.59×10^{-10}	2.09×10^{-9}	1.77×10^{-10}
Maximum (Max)	4.42×10^{-7}	1.14×10^{-7}	9.54×10^{-7}	5.90×10^{-7}
Average (Ave.)	5.64×10^{-8}	1.77×10^{-8}	1.31×10^{-7}	8.11×10^{-8}
Median (Med.)	2.13×10^{-8}	8.61×10^{-9}	6.52×10^{-8}	3.13×10^{-8}

both molecules are derived in IRAS 18182-1433 HMC1. The excitation temperature at HMC1 is the highest value ($\approx 278 \text{ K}$) among the observed hot cores. This is consistent with the agreement of the maximum abundance with the highest T_{max} model. On the other hand, HMC2 and HMC3 in the same region do not show high abundances, and NH₂CHO has not been detected at HMC3. Hence, in this high-mass star-forming region, it is likely that a massive young stellar object (MYSO) in HMC1

was first born rapidly, and the other sources were slowly formed later.

The average and median values of HNCO and NH₂CHO are consistent with the models with $T_{\text{max}} = 150\text{--}400 \text{ K}$. The best agreed conditions are $t_{\text{coll}} = (2\text{--}3) \times 10^5 \text{ yr}$, and the models with lower T_{max} values need to collapse quickly.

In the case of H₂CO, the minimum observed abundance agrees with the models within 1 order of magnitude except for

$T_{\max} = 400$ K, but the other three representative values disagree with the models. This could be explained by the fact that the observed H_2CO abundances prefer the models with low- ρ_{\max} values, while the right panels show results with $\rho_{\max} = 10^7 \text{ cm}^{-3}$.

The observed CH_3CN abundances disagree in most cases, but CH_3CN does not take part in the formation network of NH_2CHO . This disagreement does not undermine our analysis for NH_2CHO . The minimum value agrees with the models of $T_{\max} = 100$ K and $t_{\text{coll}} \approx (3-6) \times 10^5$ yr within 1 order of magnitude. As seen in Figure 10 in Appendix C, the observed CH_3CN abundances agree with the modeled maximum abundances with low- ρ_{\max} models ($10^5 - 10^{5.5} \text{ cm}^{-3}$), not at the end of the simulations. This could mean that CH_3CN is deficient at the age of the end of the simulations due to its destruction, and the CH_3CN gas may trace chemically younger gas around MYSOs.

We note that there are still uncertainties in the reaction rate constants for the dual-cyclic hydrogen addition and abstraction reactions. We tested changing the α value by 2 orders of magnitude (from $\alpha = 10^{-10}$ to $\alpha = 10^{-12}$). The modeled HNCO abundance becomes lower by 3 orders of magnitude, and the NH_2CHO abundance increase by 1 order of magnitude. Hence, the modeled HNCO abundance with $\alpha = 10^{-12}$ cannot explain the observed abundances, and the rate constants used by Gorai et al. (2020), $\alpha = 10^{-10}$, seem to be more reasonable. However, measurements to estimate the rate constants of the reactions involved are necessary to better understand relationships among these species in various astronomical environments.

In summary, most of the sources observed by the DIHCA project are at the hot core stage with temperatures of 150–400 K and densities of 10^6 – 10^7 cm^{-3} , judging from HNCO and NH_2CHO . These values are consistent with typical hot core values. On the other hand, the observed H_2CO and CH_3CN abundances prefer models with lower density conditions of $\sim 10^5$ – $10^{5.5} \text{ cm}^{-3}$. This is consistent with the spatial distribution of the observed emission. Thus, the contribution from the outer parts of cores is larger in the case of H_2CO and CH_3CN , while NH_2CHO and HNCO emission comes from inner central cores. These are consistent with the expectation based on the calculated binding energy as discussed in Section 4.2.

5. Conclusions

We have analyzed molecular lines of NH_2CHO , HNCO, H_2CO , and CH_3CN ($^{13}\text{CH}_3\text{CN}$) toward the 30 high-mass star-forming regions targeted by the DIHCA project. The angular resolutions of $\sim 0''.3$ spatially resolve hot molecular cores (HMCs). The main conclusions of this paper are as follows.

1. The lines of CH_3CN , HNCO, and H_2CO have been detected from 29 high-mass star-forming regions (96.7%), and the lines of NH_2CHO have been detected from 23 regions (76.7%). Thanks to a large number of detections of the target species, we statistically investigated their chemical links. A total of 44 HMCs have been identified in the moment 0 maps of CH_3CN .
2. The identified cores have the excitation temperatures of ~ 62 – 278 K and H_2 column densities of 1.7×10^{23} – $2.9 \times 10^{25} \text{ cm}^{-2}$, respectively. We have derived molecular abundances with respect to H_2 .
3. We have investigated correlations between NH_2CHO and HNCO and between NH_2CHO and H_2CO by applying a partial correlation test in order to investigate pure chemical links excluding a possible lurking third variable (temperature

in this case). The derived correlation coefficients are 0.89 and 0.84 for pairs of NH_2CHO –HNCO and NH_2CHO – H_2CO , respectively. These strong correlations indicate that they are most likely chemically linked in hot cores.

4. We have fitted the abundance plots of HNCO versus NH_2CHO and H_2CO versus NH_2CHO . We have obtained the best power-law fit of $X(\text{NH}_2\text{CHO}) = 0.07X(\text{HNCO})^{0.92}$, which is well consistent with a previous study ($X(\text{NH}_2\text{CHO}) = 0.04X(\text{HNCO})^{0.93}$; López-Sepulcre et al. 2015). Their abundances studied in this paper are higher than those of previous studies, and then we have confirmed that this relationship is applicable in a wide range of their abundances. The same power-law fit from low- to high-mass star-forming regions suggest that chemistry of NH_2CHO is common around YSOs with various stellar masses. The best power-law fit for the plot of H_2CO versus NH_2CHO is $X(\text{NH}_2\text{CHO}) = 0.35X(\text{H}_2\text{CO})^{1.07}$.
5. We have compared the observed abundances and chemical models including the dual-cyclic hydrogen addition and abstraction reactions between HNCO and NH_2CHO and the gas-phase formation of NH_2CHO by the reaction between NH_2 and H_2CO . The models can reproduce the observed molecular abundances. The observed abundances of HNCO and NH_2CHO prefer the models with temperatures of 150–400 K and densities of 10^6 – 10^7 cm^{-3} , which agree with typical hot core values. On the other hand, the H_2CO and CH_3CN abundances prefer the models with lower maximum densities ($\sim 10^5$ – $10^{5.5} \text{ cm}^{-3}$). These results mean that the HNCO and NH_2CHO emission comes from inner cores, whereas the contributions from the outer part of cores are mixed in the case of the H_2CO and CH_3CN emission. This scenario is consistent with the spatial distributions of each species (the H_2CO and CH_3CN emission is more extended than the other two species) and the calculated binding energies.

This paper makes use of the following ALMA data: ADS/JAO.ALMA#2016.1.01036.S and 2017.1.00237.S. ALMA is a partnership of ESO (representing its member states), NSF (USA), and NINS (Japan), together with NRC (Canada), MOST and ASIAA (Taiwan), and KASI (Republic of Korea), in cooperation with the Republic of Chile. The Joint ALMA Observatory is operated by ESO, AUI/NRAO, and NAOJ. K. T. is supported by JSPS KAKENHI grant No. JP20K14523. K.T. was supported by the ALMA Japan Research Grant of NAOJ ALMA Project, NAOJ-ALMA-278. P.S. was partially supported by a Grant-in-Aid for Scientific Research (KAKENHI Number JP22H01271 and JP23H01221) of the Japan Society for the Promotion of Science (JSPS). P.G. acknowledges the support from the Chalmers Initiative of Cosmic Origins Postdoctoral Fellowship. Data analysis was in part carried out on the Multi-wavelength Data Analysis System operated by the Astronomy Data Center (ADC), National Astronomical Observatory of Japan. We thank the anonymous referee whose valuable comments helped improve the paper.

Facility: Atacama Large Millimeter/submillimeter Array (ALMA).

Software: Common Astronomy Software Applications package (CASA; CASA Team et al. 2022), CASSIS (Vastel et al. 2015).

Appendix A

Spatial Distributions of Each Molecule

Figures 9(a)–(d) show the moment 0 maps of molecular lines (contours) overlaid on continuum images (gray scale). Red crosses indicate the positions of hot molecular cores (HMCs) identified in the moment 0 maps of CH_3CN . If there is one HMC in a high-mass star-forming region, we did not indicate numbers. We

labeled numbers for HMCs in order of integrated intensity, from the highest to the lowest, if several HMCs are identified in a high-mass star-forming region. Tables 8 and 9 summarize information on noise level and contour levels of each panel. The same contour levels are applied for the same regions. The line of H_2CO is contaminated with another line in two HMCs (G351.77-0.54 and NGC6334I), and we could not make its moment 0 maps.

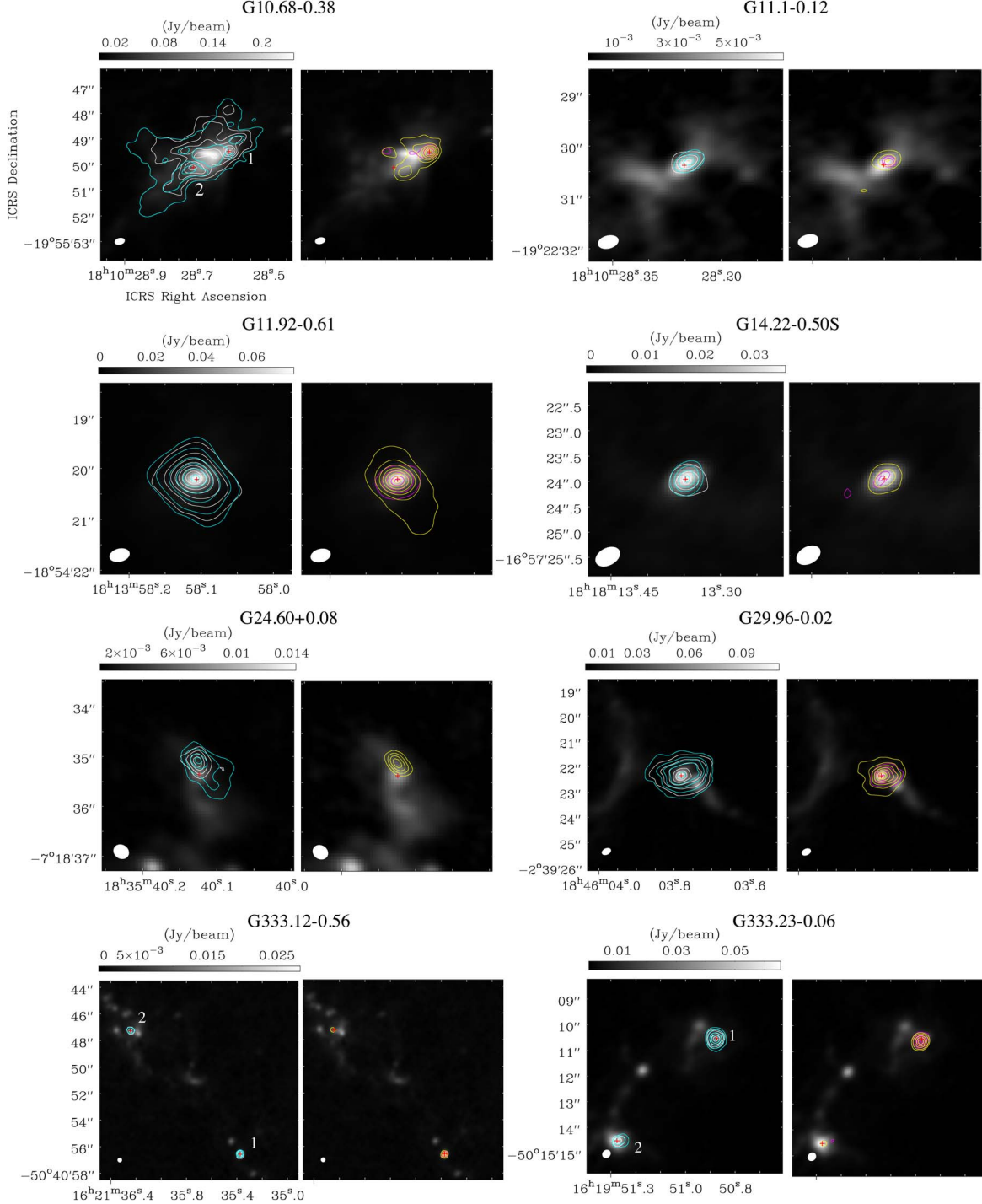


Figure 9. Continuum images (gray scales) overlaid with contours indicating moment 0 maps of molecular lines (left panels: white; CH_3CN and cyan; H_2CO , right panels: magenta; NH_2CHO and yellow; HNC). Red crosses indicate positions of hot molecular cores (HMCs). Information on noise levels and contour levels are summarized in Tables 8 and 9.

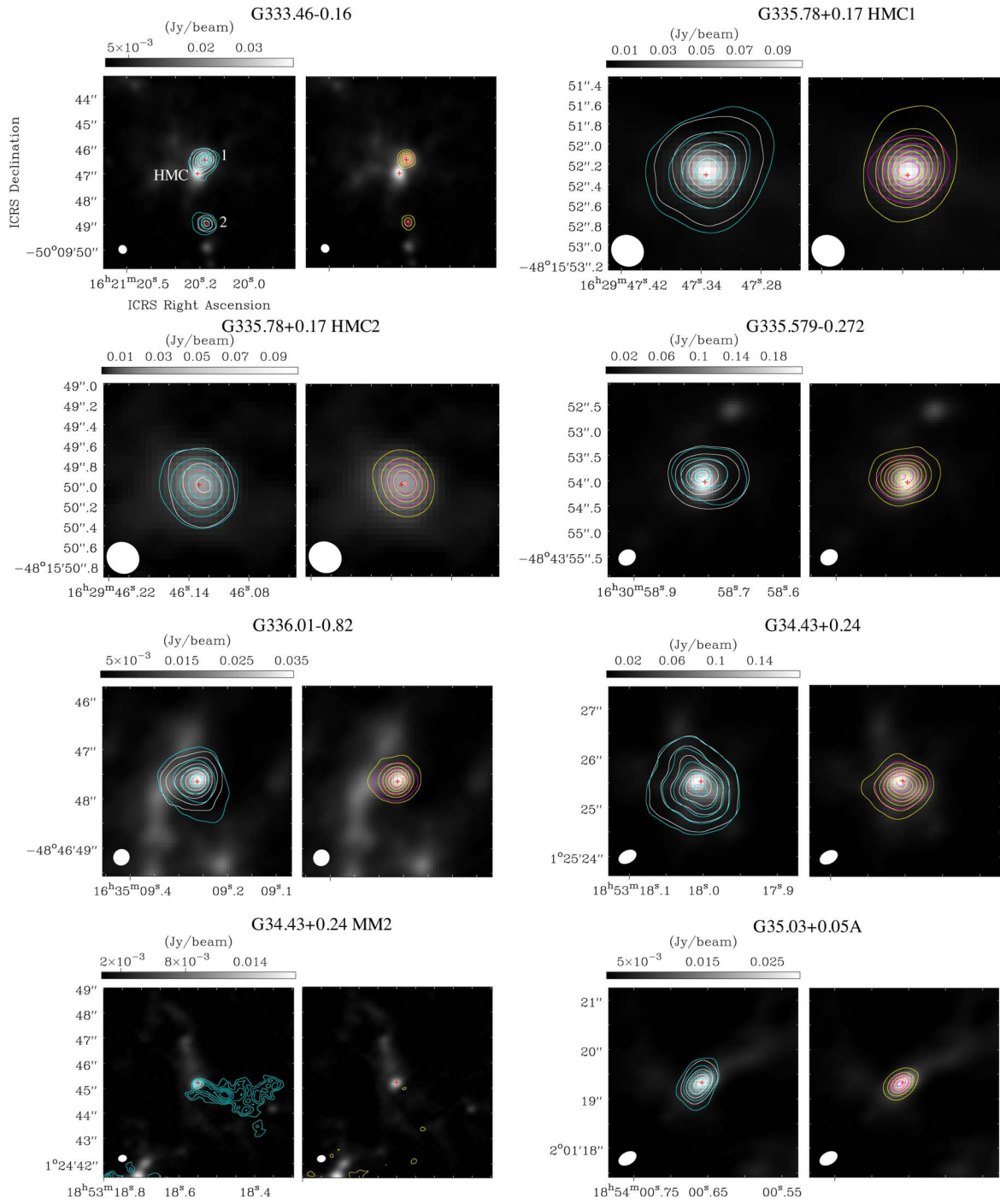


Figure 9. (Continued.)

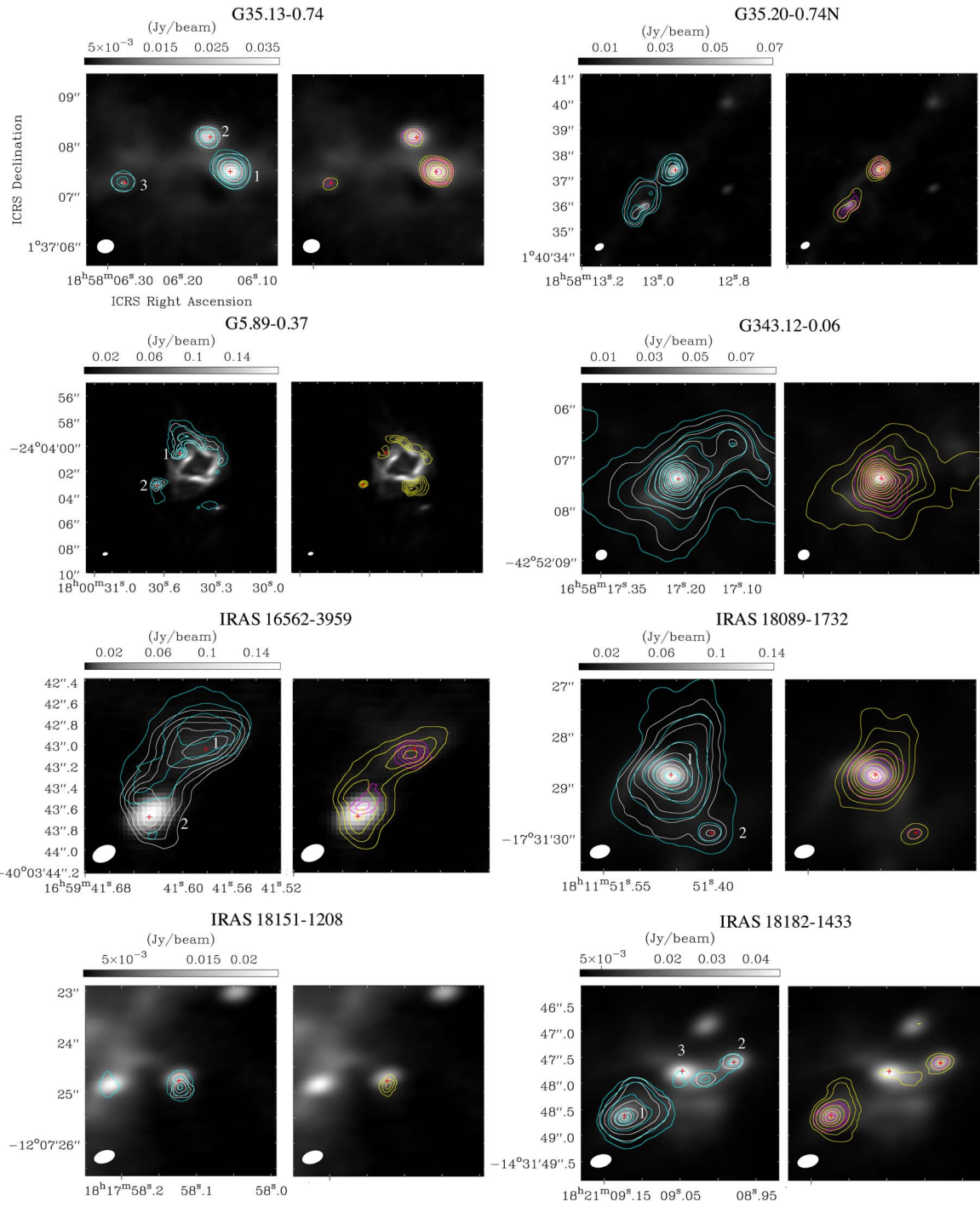


Figure 9. (Continued.)

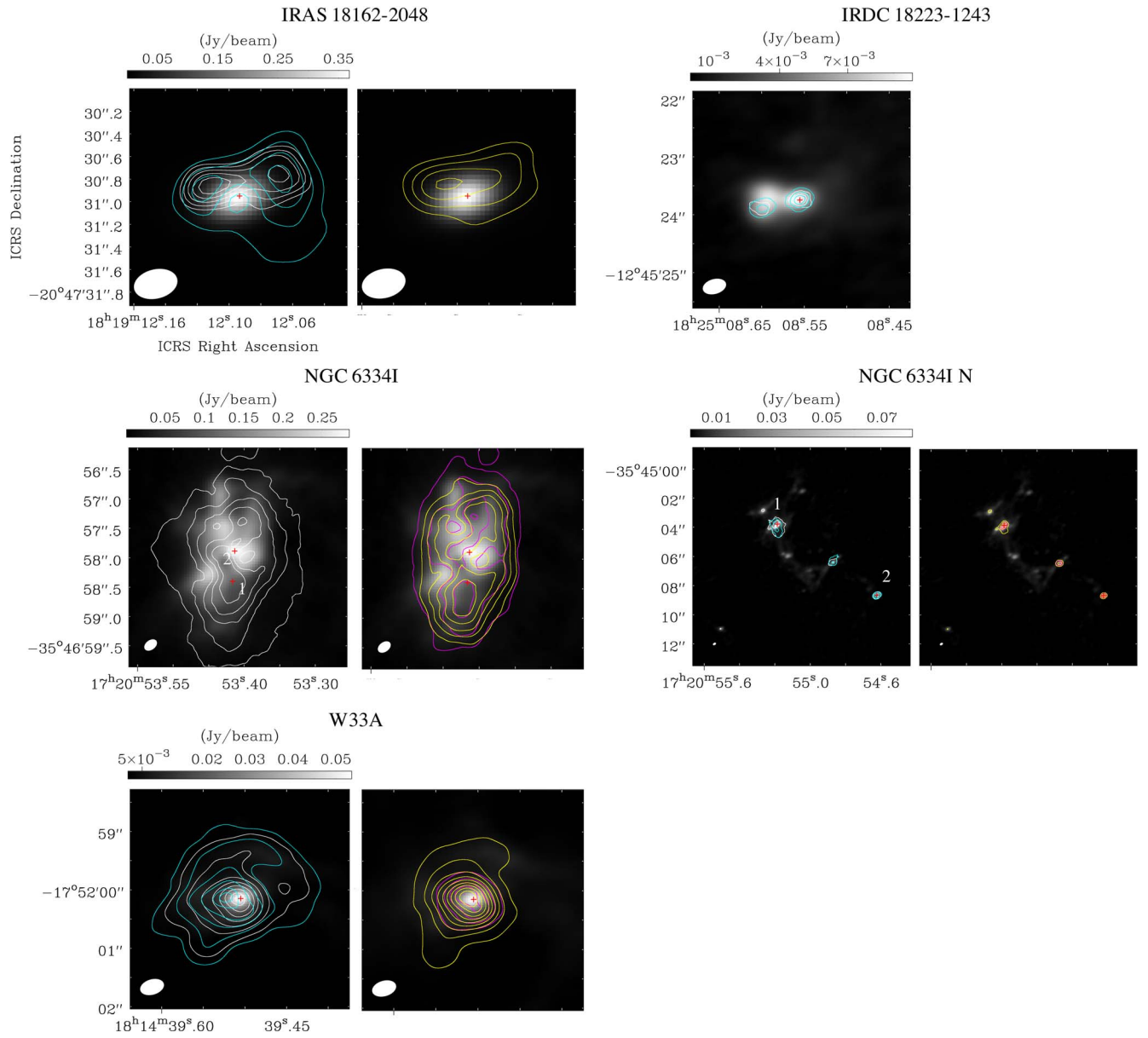


Figure 9. (Continued.)

Table 8
Information on Noise Level of Continuum Image and Moment 0 Maps

Region	Position	R.A.	Decl.	Continuum	CH ₃ CN	H ₂ CO	HNCO	NH ₂ CHO
G10.62-0.38	HMC1	18:10:28.61	−19:55:49.487	0.47	0.04	0.031	0.032	0.028
	HMC2	18:10:28.709	−19:55:50.099					
G11.1-0.12	HMC	18:10:28.25	−19:22:30.372	0.1	0.033	0.025	0.025	0.026
G11.92-0.61	HMC	18:13:58.106	−18:54:20.213	0.14	0.043	0.031	0.034	0.028
G14.22-0.50 S	HMC	18:18:13.348	−16:57:23.955	0.2	0.038	0.032	0.024	0.016
G24.60+0.08	HMC	18:35:40.124	−7:18:35.356	0.081	0.025	0.023	0.016	...
G29.96-0.02	HMC	18:46:03.781	−2:39:22.352	0.35	0.072	0.041	0.057	0.043
G333.12-0.56	HMC1	16:21:35.374	−50:40:56.555	0.15	0.036	0.032	0.028	0.045
	HMC2	16:21:36.242	−50:40:47.252					
G333.23-0.06	HMC1	16:19:50.875	−50:15:10.526	0.23	0.05	0.039	0.044	0.033
	HMC2	16:19:51.276	−50:15:14.522					
G333.46-0.16	HMC	16:21:20.211	−50:09:46.985	0.18	0.037	0.025	0.023	0.022
	HMC1	16:21:20.182	−50:09:46.455					
	HMC2	16:21:20.171	−50:09:48.957					
G335.579-0.272	HMC	16:30:58.758	−48:43:54.011	0.45	0.052	0.036	0.039	0.038
G335.78+0.17	HMC1	16:29:47.335	−48:15:52.296	0.28	0.042	0.029	0.03	0.032
	HMC2	16:29:46.130	−48:15:49.982					
G336.01-0.82	HMC	16:35:09.262	−48:46:47.638	0.21	0.043	0.024	0.034	0.029
G34.43+0.24	HMC	18:53:18.005	1:25:25.524	0.39	0.067	0.045	0.047	0.04
G34.43+0.24 MM2	HMC	18:53:18.552	1:24:45.228	0.2	0.019	0.024	0.012	...
G35.03+0.35A	HMC	18:54:00.658	2:01:19.330	0.16	0.056	0.033	0.038	0.031
G35.13-0.74	HMC1	18:58:06.135	1:37:07.476	0.17	0.03	0.03	0.024	0.02
	HMC2	18:58:06.163	1:37:08.167					
	HMC3	18:58:06.278	1:37:07.247					
G35.20-0.74N	HMC	18:58:12.952	1:40:37.357	0.22	0.043	0.037	0.043	0.036
G351.77-0.54	HMC	17:26:42.531	−36:09:17.376	1.0	0.059	... ^a	0.04	0.024
G5.89-0.37	HMC1	18:00:30.507	−24:04:00.561	0.44	0.058	0.061	0.042	...
	HMC2	18:00:30.639	−24:04:03.082					
G343.12-0.06	HMC	16:58:17.212	−42:52:07.402	0.19	0.036	0.024	0.025	0.019
IRAS 16562-3959	HMC1	16:59:41.581	−40:03:43.047	0.2	0.028	0.017	0.017	0.013
	HMC2	16:59:41.627	−40:03:43.691					
IRAS 18089-1732	HMC1	18:11:51.457	−17:31:28.771	0.23	0.044	0.025	0.029	0.026
	HMC2	18:11:51.403	−17:31:29.919					
IRAS 18151-1208	HMC	18:17:58.123	−12:07:24.775	0.1	0.018	0.013	0.0087	...
IRAS 18182-1433	HMC1	18:21:09.123	−14:31:48.644	0.14	0.025	0.019	0.022	0.015
	HMC2	18:21:08.979	−14:31:47.590					
	HMC3	18:21:09.047	−14:31:47.775					
IRAS 18162-2048	HMC	18:19:12.093	−20:47:30.946	0.32	0.033	0.033	0.027	...
IRDC 18223-1243	HMC	18:25:08.554	−12:45:23.748	0.074	0.02	0.013
NGC6334I	HMC1	17:20:53.416	−35:46:58.397	1.2	0.072	... ^a	0.11	0.031
	HMC2	17:20:53.413	−35:46:57.881					
NGC6334I N	HMC1	17:20:55.186	−35:45:03.781	0.51	0.035	0.021	0.028	0.019
	HMC2	17:20:54.623	−35:45:08.653					
W33A	HMC	18:14:39.505	−17:52:00.147	0.17	0.047	0.029	0.033	0.026

Notes. Units are mJy beam^{−1} and Jy beam^{−1} km s^{−1} for continuum images and moment 0 maps of molecular lines, respectively. The position names and their coordinates are provided as a machine-readable table.

^a Moment 0 maps could not be made due to line contamination.

(This table is available in machine-readable form.)

Table 9
Information on Contour Levels of Continuum Image and Moment 0 Maps

Region	CH ₃ CN	H ₂ CO	HNCO	NH ₂ CHO
G10.62-0.38	10–60 (10 step)	10, 20, 30	10–70 (10 step)	10, 20, 30
G11.1-0.12	5, 10, 15	10, 15, 20	5, 10, 15	4, 5
G11.92-0.61	10–150 (20 step)	10, 20, 40, 60, 80, 100	10–130 (20 step)	10, 30, 50, 70, 80
G14.22-0.50 S	5, 10, 14	10, 15, 20, 24	5, 10, 15	4, 5
G24.60+0.08	5, 7, 9, 11	7, 10, 15, 18	5, 7, 9, 11, 13	...
G29.96-0.02	10–130 (20 step)	10–110 (20 step)	10–110 (20 step), 120	10–90 (20 step)
G333.12-0.56	10, 20, 30	10, 15, 20, 25	10, 20, 30	5, 7, 10
G333.23-0.06	10, 15, 25, 35, 45	10, 15, 25, 35, 45	10, 15, 25, 35, 45	4–24 (4 step)
G333.46-0.16	10–60 (10 step)	10, 20, 30, 35	10–50 (10 step)	10, 20, 30
G335.579-0.272	20–100 (20 step), 110	20, 40, 60, 70	10–130 (20 step), 140	10, 30, 50, 70
G335.78+0.17 HMC1	10–90 (20 step)	10, 30, 50, 70	10–110 (20 step)	10–50 (10 step)
G335.78+0.17 HMC2	10, 30, 50	10, 20, 30, 40	10, 20, 30, 40, 50	10, 15, 20, 25
G336.01-0.82	10, 20–100 (20 step)	10–70 (20 step)	10–110 (20 step)	10, 30, 50, 70
G34.43+0.24	10–110 (20 step)	10–90 (20 step)	10–130 (20 step)	10–90 (20 step)
G34.43+0.24 MM2	5, 6, 7	5, 6, 7, 8, 9, 10	3, 4, 5	...
G35.03+0.35A	10, 20, 30, 40	10, 20, 30, 40	10, 20, 30, 40	10, 12, 15, 18
G35.13-0.74	10, 20, 30, 40, 50	10, 15, 20, 30	10, 15, 20, 30, 40, 50	5, 7, 10, 20, 30
G35.20-0.74N	10, 30, 50, 70	10, 20, 30, 40	10, 20, 30, 50, 70, 80	5, 10, 20, 30, 40
G351.77-0.54	10–230 (20 step)	... ^a	10–210 (20 step)	10–90 (20 step)
G5.89-0.37	10, 20, 30, 40	10, 20, 30, 35	10, 15, 20, 25, 30, 35	...
G343.12-0.06	10–230 (20 step)	10–150 (20 step)	10–230 (20 step)	10–130 (20 step)
IRAS 16562-3959	10, 15, 20, 25, 30	10, 15, 20	10, 15, 20, 25	5, 7, 9, 11, 13
IRAS 18089-1732	10, 20, 30–150 (20 step)	10, 30, 50, 70, 90, 100	10, 20–100 (20 step), 150, 200	10–90 (20 step), 100
IRAS 18151-1208	5, 7, 9, 11	10, 20, 30	5, 7, 9	...
IRAS 18182-1433	10, 20, 40, 60, 80, 90	10, 15, 30, 50, 60	5, 10, 20, 40, 60, 80, 100	5, 10, 30, 50, 60
IRAS 18162-2048	10, 12, 14, 16, 18	10, 15, 20, 25	10, 15, 20, 25	...
IRDC 18223-1243	5, 7, 9, 11	10, 15, 20
NGC6334I	10, 15, 20, 25, 30	... ^a	10, 15, 20, 25, 30	10, 30, 50, 60
NGC6334I N	10, 30, 50	10, 20, 30	10, 30, 50	10, 20, 30
W33A	10–130 (20 step), 140	10–90 (20 step), 100	10–210 (20 step)	10–110 (20 step)

Note.

^a Moment 0 maps could not be made due to line contamination.

Appendix B

Velocity Component and Line Width Derived by the MCMC Method

Table 10 summarizes V_{LSR} and FWHM of each molecular line at each core derived from the MCMC method in the CASSIS software. In the fitting, the initial guess of V_{LSR} is based on the CH₃CN line data, and we set the range of $V_{\text{LSR}} = \pm 3 \text{ km s}^{-1}$ from the initial guess in the MCMC analysis.

Table 10
Velocity Component and FWHM Derived by the MCMC Method

Region	Position	$^{13}\text{CH}_3\text{CN}$		NH_2CHO		HNCO		H_2CO	
		V_{LSR}	FWHM	V_{LSR}	FWHM	V_{LSR}	FWHM	V_{LSR}	FWHM
G10.62-0.38	HMC1	0.851 (3)	5.041 (6)	1.71 (1)	6.0 (4)	0.042 (1)	5.866 (4)	−1.318 (2)	3.392 (4)
	HMC2	−3.194 (1)	2.646 (3)	−2.805 (2)	3.302 (4)	−3.142 (1)	3.187 (3)
G11.1-0.12	HMC	31.85 (2)	4.24 (1)	32.97 (7)	3.4 (3)	31.404 (3)	7.38 (5)	31.57 (1)	4.49 (3)
G11.92-0.61	HMC	35.1000 (3)	10.8 (2)	35.6 (1)	9.9 (8)	34.331 (1)	13.594 (3)	34.8 (1)	7.6 (5)
G14.22-0.50 S	HMC	22.698 (8) ^a	6.23 (2) ^a	25.44 (3)	5.91 (2)	22.28 (1)	9.07 (7)	23.070 (5)	4.47 (1)
G24.60+0.08	HMC	52.5 (2) ^a	4.7 (4) ^a	54.05 (4)	17.65 (8)	52.87 (1)	7.19 (3)
G29.96-0.02	HMC	97.246 (1)	7.976 (3)	97.097 (3)	9.0 (1.2)	96.4 (5)	9.0 (1.8)	96.0 (2)	8.29 (1)
G333.12-0.56	HMC1	−58.47 (2)	11.5 (3)	−57.16 (2)	9.77 (2)	−59.850 (5)	11.52 (1)	−60.56 (1)	7.17 (3)
	HMC2	−54.10 (6)	4.02 (1)	−53.93 (1)	6.03 (1)	−55.167 (5)	6.01 (1)	−52.8 (2)	4.9 (3)
G333.23-0.06	HMC1	−87.04 (5)	4.3 (3)	−86.5 (1)	6.9 (3)	−87.29 (4)	7.3 (1.9)	−87.49 (1)	8.999 (1)
	HMC2	−84.96 (2)	4.1 (7)	−84.8 (3)	5.5 (4)	−85.200 (1)	9.96 (3)	−85.12 (3)	6.990 (8)
G333.46-0.16	HMC	−44.057 (7)	3.95 (2)	−41.61 (1)	8.9994 (3)	−44.728 (4)	3.54 (1)
	HMC1	−43.55 (2)	4.03 (1)	−42.409 (3)	5.271 (8)	−43.261 (2)	5.84 (5)	−44.81 (1)	2.0 (3)
	HMC2	−39.23 (4)	3.9 (1)	−39.94 (4)	7.4 (4)	−42.446 (5)	9.74 (1)	−40.997 (2)	7.72 (2)
		−45.15 (2) ^b	3.87 (9) ^b
G335.579-0.272	HMC	−46.44 (7)	3.2 (7)	−45.82 (4)	5.5 (6)	−47.21 (1)	6.7 (1.0)
G335.78+0.17	HMC1	−48.94 (6)	8.304 (4)	−48.990 (3)	9.144 (9)	−51.1 (1)	10.0 (1.1)	−49.37 (6)	11.999 (4)
	HMC2	−50.51 (9)	7.8 (1)	−50.769 (5)	8.51 (1)	−51.80 (7)	8.4 (1.1)	−50.654 (5)	8.34 (1)
G336.01-0.82	HMC	−47.186 (8)	10.01 (9)	−45.665 (2)	10.492 (5)	−46.2 (2)	9.9 (2)
G34.43+0.24	HMC	58.440 (2)	7.5 (2)	59.3 (2)	6.11 (7)	58.5 (2)	8.8 (4)
G34.43 +0.24 MM2	HMC	55.502 (2) ^a	4.8 (1) ^a	55.86 (4)	3.61 (6)	55.41 (2)	7.988 (9)
G35.03+0.35A	HMC	45.94 (2)	5.91 (7)	45.342 (2)	4.14 (4)	45.71 (1)	6.4 (2.2)	47.733 (3)	7.140 (6)
G35.13-0.74	HMC1	35.93 (2)	7.67 (5)	31.57 (2)	7.0 (2)	31.6 (4)	2.6 (9)
				38.00(1) ^b	4.14 (5) ^b	36.73 (4) ^b	3.6 (6) ^b
	HMC2	34.39 (2)	8.54 (9)	36.1 (1)	7.1 (6)	34.031 (9)	11.00 (3)	34.585 (9)	7.85 (2)
	HMC3	35.527 (6) ^a	4.65 (4) ^a	33.91 (3)	8.00 (1)	34.758 (5)	6.16 (2)	36.205 (5)	5.23 (1)
G35.20-0.74 N	HMC	32.113 (3)	5.165 (8)	32.13 (4)	6.4 (5)	31.602 (3)	6.973 (5)	31.43 (9)	4.66 (9)
G351.77-0.54	HMC	−3.825 (1)	9.127 (3)	−2.538 (1)	6.708 (4)	−2.53 (8)	2.9 (6)
G5.89-0.37	HMC1	11.132 (3)	5.24 (1)	11.808 (4)	6.825 (8)	11.5 (2)	7.5 (3)
	HMC2	7.918 (9)	6.47 (2)	8.54 (3)	7.13 (3)	9.189 (2)	5.529 (5)
G343.12-0.06	HMC	−33.708 (3)	9.09 (4)	−32.77 (3)	5.02 (7)	−32.01 (1)	6.2 (5)	−33.124 (5)	7.215 (6)
IRAS 16562-3959	HMC1	−14.233 (1)	3.897 (6)	−13.222 (1)	3.536 (3)	−13.722 (4)	3.176 (2)	−14.90 (5)	3.1 (3)
	HMC2	−16.86 (2)	4.9998 (2)	−17.142 (4)	6.482 (8)	−17.3 (2)	6.7 (2)	−17.207 (5)	6.54 (1)
IRAS 18089-1732	HMC1	32.875 (3)	7.88 (8)	32.36 (4)	7.5 (3)	31.55 (3)	7.8 (1.8)	34.20 (1)	5.8 (3)
	HMC2	33.02 (6)	8.0 (1)	33.399 (1)	10.67 (5)	33.172 (6)	10.88 (1)	33.743 (3)	6.177 (7)
IRAS 18151-1208	HMC	30.410 (2) ^a	2.95 (2) ^a	30.073 (5)	3.48 (1)	30.520 (2)	3.030(5)
IRAS 18182-1433	HMC1	61.12 (2)	8.51 (3)	61.7 (3)	6.9 (1.8)	59.8 (2)	9.9 (2)	60.034 (2)	7.647 (5)
	HMC2	60.635 (8)	4.67 (1)	61.0 (1)	6.1 (1.2)	60.59 (3)	5.3 (1.1)	61.038 (4)	5.20 (1)
	HMC3	62.78 (1)	4.64 (3)	61.94 (2)	7.9994 (5)	63.398 (8)	2.9998 (2)
IRAS 18162-2048	HMC	13.816 (2) ^a	5.843 (6) ^a	13.8 (3)	4.5 (1.0)	14.745 (2)	2.561 (6)
IRDC 18223-1243	HMC	45.685 (8) ^a	6.55 (5) ^a	45.84 (2)	9.05 (6)	45.532 (5)	5.35 (2)
NGC6334I N	HMC1	−1.768 (2)	7.37 (1)	−0.699 (3)	7.44 (1)	−2.6 (7)	7.0 (1.6)
	HMC2	−7.59 (6)	3.6 (2)	−5.547 (3)	10.529 (6)	−6.47 (6)	6.6 (1.2)	−7.47 (2)	4.374 (7)
W33A	HMC	37.939 (3)	8.55 (2)	39.53 (2)	9.32 (1)	38.51 (2)	6.3 (5)	38.802 (1)	6.938 (3)

Notes. Unit is km s^{-1} . The numbers in parentheses indicate the standard deviation derived from the MCMC analysis, expressed in units of the last significant digits.

^a Derived from fitting of the lines of CH_3CN .

^b Applied by two velocity-component fitting.

Appendix C

Comparison with Peak Abundances of Model B

Figure 10 shows comparisons of observational results with the modeled maximum abundances obtained by Model B (Gorai et al. 2020).

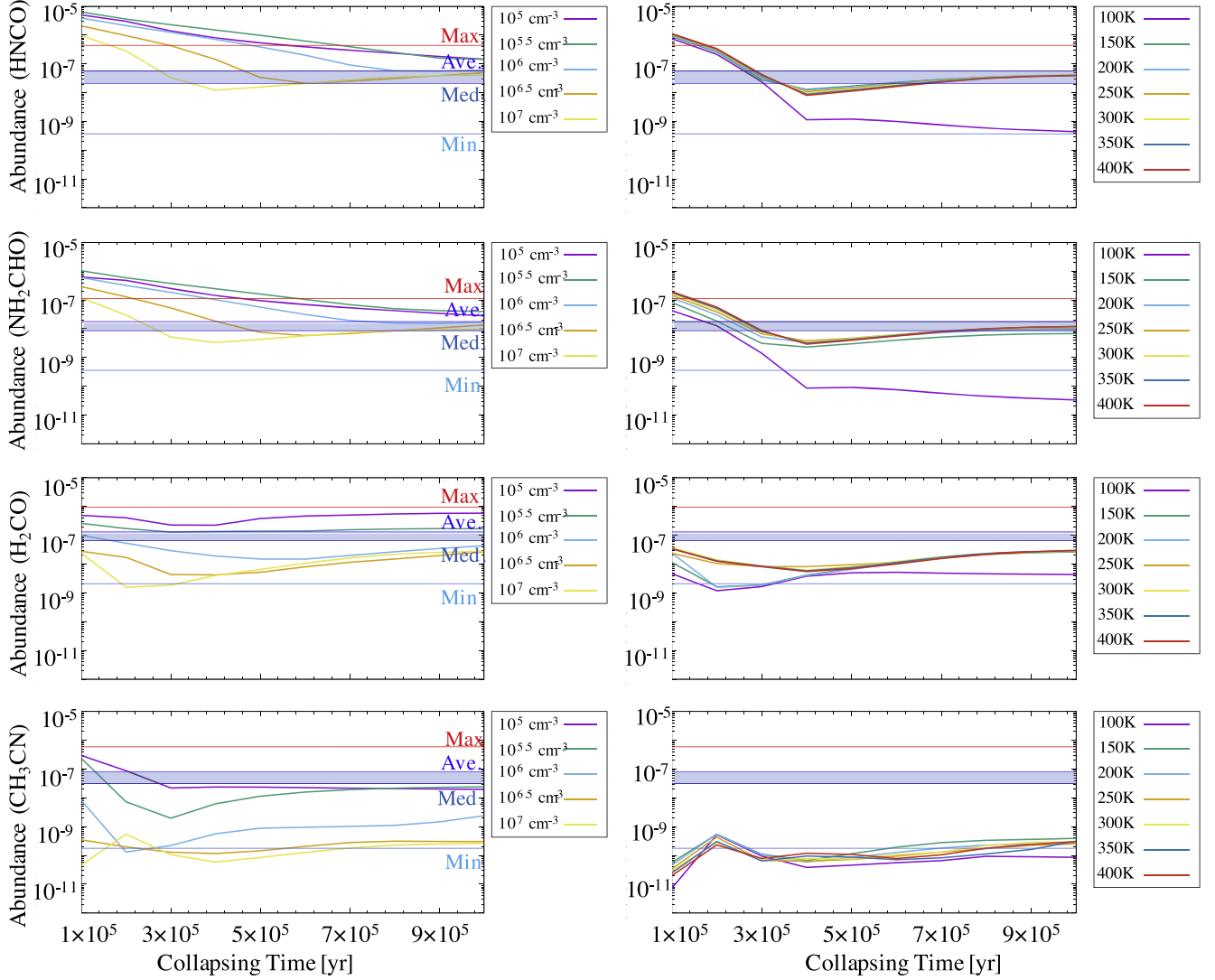





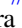







Figure 10. Comparison with the maximum abundances of Model B (Gorai et al. 2020). The panels from top to bottom show the results of HNCO, NH₂CHO, H₂CO, and CH₃CN, respectively. The left panels show the dependences on different collapsing timescales and maximum densities. The right panels show the dependences on different collapsing timescales and maximum temperatures with a maximum density of 10⁷ cm⁻³. The four representative observed abundances are plotted (Maximum, Median, and Minimum). The blue filled ranges indicate the ranges between the average and median values.

ORCID iDs

Kotomi Taniguchi  <https://orcid.org/0000-0003-4402-6475>
 Patricio Sanhueza  <https://orcid.org/0000-0002-7125-7685>
 Fernando A. Olguin  <https://orcid.org/0000-0002-8250-6827>
 Prasanta Gorai  <https://orcid.org/0000-0003-1602-6849>
 Ankan Das  <https://orcid.org/0000-0003-4615-602X>
 Fumitaka Nakamura  <https://orcid.org/0000-0001-5431-2294>
 Masao Saito  <https://orcid.org/0000-0003-0769-8627>
 Qizhou Zhang  <https://orcid.org/0000-0003-2384-6589>
 Xing Lu  <https://orcid.org/0000-0003-2619-9305>
 Shanghuo Li  <https://orcid.org/0000-0003-1275-5251>
 Huei-Ru Vivien Chen  <https://orcid.org/0000-0002-9774-1846>

References

- Barone, V., Latouche, C., Skouteris, D., et al. 2015, *MNRAS*, **453**, L31
 Belloche, A., Meshcheryakov, A. A., Garrod, R. T., et al. 2017, *A&A*, **601**, A49
 Carrasco-González, C., Rodríguez, L. F., Anglada, G., et al. 2010, *Sci*, **330**, 1209
 CASA Team, Bean, B., Bhatnagar, S., et al. 2022, *PASP*, **134**, 114501
 Chuang, K.-J., Jäger, C., Krasnokutski, S. A., Fulvio, D., & Henning, Th. 2022, *ApJ*, **933**, 107
 Contreras, Y. 2018, Automatic Line Clean, Zenodo, doi:10.5281/zenodo.1216881
 Contreras, Y., Sanhueza, P., Jackson, J. M., et al. 2018, *ApJ*, **861**, 14
 Dulieu, F., Nguyen, T., Congiu, E., Baouche, S., & Taquet, V. 2019, *MNRAS Lett.*, **484**, L119
 Eisenhauer, F., Schödel, R., Genzel, R., et al. 2003, *ApJL*, **597**, L121
 Endres, C. P., Schlemmer, S., Schilke, P., Stutzki, J., & Müller, H. S. P. 2016, *JMoSp*, **327**, 95
 Enrique-Romero, J., Rimola, A., Ceccarelli, C., et al. 2019, *ESC*, **3**, 2158
 Enrique-Romero, J., Rimola, A., Ceccarelli, C., et al. 2022, *ApJS*, **259**, 39
 Fedoseev, G., Chuang, K.-J., van Dishoeck, E. F., Ioppolo, S., & Linnartz, H. 2016, *MNRAS*, **460**, 4297
 Fernández-López, M., Sanhueza, P., Zapata, L. A., et al. 2021, *ApJ*, **913**, 29
 Ferrero, S., Zamirri, L., Ceccarelli, C., et al. 2020, *ApJ*, **904**, 11
 Giannetti, A., Leurini, S., König, C., et al. 2017, *A&A*, **606**, L12
 Girart, J. M., Estalella, R., Fernández-López, M., et al. 2017, *ApJ*, **847**, 58
 Gorai, P., Bhat, B., Sil, M., et al. 2020, *ApJ*, **895**, 86
 Guzmán, A. E., Guzmán, V. V., Garay, G., Bronfman, L., & Hechenleitner, G. 2018, *ApJS*, **236**, 45
 Haupa, K. A., Tarczay, G., & Lee, Y.-P. 2019, *JACHS*, **141**, 11614
 Hernández-Hernández, V., Zapata, L., Kurtz, S., & Garay, G. 2014, *ApJ*, **786**, 38
 Hollis, J. M., Lovas, F. J., Remijan, A. J., et al. 2006, *ApJL*, **643**, L25
 Hunter, T. R., Brogan, C. L., Cyganowski, C. J., & Young, K. H. 2014, *ApJ*, **788**, 187
 Jones, B. M., Bennett, C. J., & Kaiser, R. I. 2011, *ApJ*, **734**, 78
 Kauffmann, J., & Pillai, T. 2010, *ApJL*, **723**, L7
 Law, C. J., Zhang, Q., Öberg, K. I., et al. 2021, *ApJ*, **909**, 214
 Lee, C.-F., Codella, C., Ceccarelli, C., & López-Sepulcre, A. 2022, *ApJ*, **937**, 10
 Ligterink, N. F. W., El-Abd, S. J., Brogan, C. L., et al. 2020, *ApJ*, **901**, 37
 López-Sepulcre, A., Balucani, N., Ceccarelli, C., et al. 2019, *ESC*, **3**, 2122
 López-Sepulcre, A., Jaber, A. A., Mendoza, E., et al. 2015, *MNRAS*, **449**, 2438
 Martín-Doménech, R., Öberg, K. I., & Rajappan, M. 2020, *ApJ*, **894**, 98
 Mendoza, E., Lefloch, B., López-Sepulcre, A., et al. 2014, *MNRAS*, **445**, 151
 Nazari, P., Meijerhof, J. D., van Gelder, M. L., et al. 2022, *A&A*, **668**, A109
 Noble, J. A., Theule, P., Congiu, E., et al. 2015, *A&A*, **576**, A91
 Olguin, F. A., Sanhueza, P., Ginsburg, A., et al. 2022, *ApJ*, **929**, 68
 Olguin, F. A., Sanhueza, P., Guzmán, A. E., et al. 2021, *ApJ*, **909**, 199
 Ossenkopf, V., & Henning, T. 1994, *A&A*, **291**, 943
 Pickett, H. M., Poynter, R. L., Cohen, E. A., et al. 1998, *JQSRT*, **60**, 883
 Quénard, D., Jiménez-Serra, I., Viti, S., Holdship, J., & Coutens, A. 2018, *MNRAS*, **474**, 2796
 Rimola, A., Skouteris, D., Balucani, N., et al. 2018, *ESC*, **2**, 720
 Rivilla, V. M., Colzi, L., Jiménez-Serra, I., et al. 2022, *ApJL*, **929**, L11
 Rivilla, V. M., Jiménez-Serra, I., García de la Concepción, J., et al. 2021b, *MNRAS Lett.*, **506**, L79
 Rivilla, V. M., Jiménez-Serra, I., Martín-Pintado, J., et al. 2021a, *PNAS*, **118**, e2101314118
 Rubin, R. H., Swenson, G. W., Benson, R. C., Tigelaar, H. L., & Flygare, W. H. 1971, *ApJL*, **169**, L39
 Sabatini, G., Bovino, S., Sanhueza, P., et al. 2022, *ApJ*, **936**, 80
 Sanhueza, P., Contreras, Y., Wu, B., et al. 2019, *ApJ*, **886**, 102
 Sanhueza, P., Jackson, J. M., Zhang, Q., et al. 2017, *ApJ*, **841**, 97
 Skouteris, D., Vazart, F., Ceccarelli, C., et al. 2017, *MNRAS Lett.*, **468**, L1
 Snyder, L. E., & Buhl, D. 1972, *ApJ*, **177**, 619
 Song, L., & Kästner, J. 2016, *PCCP*, **18**, 29278
 Taniguchi, K., Guzmán, A. E., Majumdar, L., Saito, M., & Tokuda, K. 2020, *ApJ*, **898**, 54
 Urquhart, J. S., König, C., Giannetti, A., et al. 2018, *MNRAS*, **473**, 1059
 Vastel, C., Bottinelli, S., Caux, E., Glorian, J.-M., & Boiziot, M. 2015, in SF2A-2015: Proc. Annual meeting of the French Society of Astronomy and Astrophysics, ed. F. Martins et al. (Paris: French Society of Astronomy & Astrophysics), **313**
 Wall, J. V., & Jenkins, C. R. 2012, in Practical Statistics for Astronomers, ed. J. V. Wall & C. R. Jenkins, Vol. 2012 (Cambridge: Cambridge Univ. Press)
 Yan, Y. T., Zhang, J. S., Henkel, C., et al. 2019, *ApJ*, **877**, 154